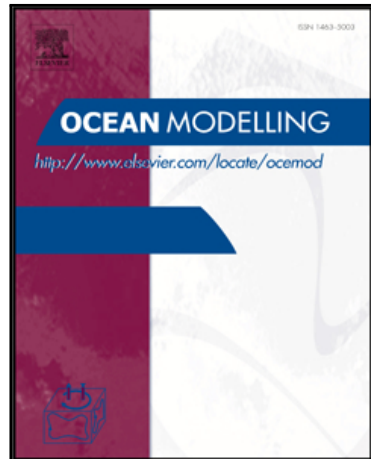


Accepted Manuscript

Seasonality of Eddy Kinetic Energy in an Eddy Permitting Global Climate Model

Takaya Uchida, Ryan Abernathey, Shafer Smith

PII: S1463-5003(17)30122-1
DOI: [10.1016/j.ocemod.2017.08.006](https://doi.org/10.1016/j.ocemod.2017.08.006)
Reference: OCEMOD 1236



To appear in: *Ocean Modelling*

Received date: 8 February 2017
Revised date: 25 July 2017
Accepted date: 14 August 2017

Please cite this article as: Takaya Uchida, Ryan Abernathey, Shafer Smith, Seasonality of Eddy Kinetic Energy in an Eddy Permitting Global Climate Model, *Ocean Modelling* (2017), doi: [10.1016/j.ocemod.2017.08.006](https://doi.org/10.1016/j.ocemod.2017.08.006)

This is a PDF file of an unedited manuscript that has been accepted for publication. As a service to our customers we are providing this early version of the manuscript. The manuscript will undergo copyediting, typesetting, and review of the resulting proof before it is published in its final form. Please note that during the production process errors may be discovered which could affect the content, and all legal disclaimers that apply to the journal pertain.

1 **Highlights**

- 2 • Examined the seasonal cycle of upper-ocean mesoscale turbulence in a high resolution
3 climate model simulation.
- 4 • Seasonality in ocean mesoscale turbulence was quantified by isotropic wavenumber spec-
5 tra of surface eddy kinetic energy.
- 6 • The small-scale turbulence was most energetic during winter time at scales below 30km.
- 7 • Showed a global picture of seasonality in baroclinic available potential energy conversion
8 rates.
- 9 • The dominant cause for seasonality was baroclinic instability due to reduced stratification
10 in the winter mixed layer.

Seasonality of Eddy Kinetic Energy in an Eddy Permitting Global Climate Model

Takaya Uchida¹, Ryan Abernathey^{1,2}

1: Department of Earth and Environmental Sciences, Columbia University in the City of New York

2: Division of Ocean and Climate Physics, Lamont-Doherty Earth Observatory

Shafer Smith³

3: Center for Atmosphere Ocean Science, Courant Institute of Mathematical Sciences, New York University

205A Oceanography 61 Route 9W - PO Box 1000 Palisades, NY 10964-8000, US

Abstract

We examine the seasonal cycle of upper-ocean mesoscale turbulence in a high resolution CESM climate simulation. The ocean model component (POP) has 0.1° degree resolution, mesoscale resolving at low and middle latitudes. Seasonally and regionally resolved wavenumber power spectra are calculated for sea-surface eddy kinetic energy (EKE). Although the interpretation of the spectral slopes in terms of turbulence theory is complicated by the strong presence of dissipation and the narrow inertial range, the EKE spectra consistently show higher power at small scales during winter throughout the ocean. Potential hypotheses for this seasonality are investigated. Diagnostics of baroclinic energy conversion rates and evidence from linear quasi-geostrophic stability analysis indicate that seasonally varying mixed-layer instability is responsible for the seasonality in EKE. The ability of this climate model, which is not considered submesoscale resolving, to produce mixed layer instability although damped by dissipation, demonstrates the ubiquity and robustness of this process for modulating upper ocean EKE.

Keywords: mesoscale turbulence, seasonality, wavenumber spectra, baroclinic instability, linear stability analysis

1 . Introduction

Mesoscale turbulence is ubiquitous in the ocean and has significant impacts on the large-scale ocean circulation and its interaction with the climate (e.g. Jayne and Marotzke, 2002; Volkov *et al.*, 2008; Lévy *et al.*, 2010; Griffies *et al.*, 2015). Ocean currents are most energetic

27 in the mesoscale range, on the order of tens to a few hundred kilometers. Mesoscale turbulence
 28 is driven by baroclinic instability of the main thermocline (*Gill et al.*, 1974; *Smith*, 2007), and is
 29 relatively well described by quasi-geostrophic (QG) models (*Rhines*, 1979; *Held et al.*, 1995),
 30 in which enstrophy and energy conservation lead to the inverse cascade of energy from small
 31 to large scales (*Charney*, 1971). Below the mesoscale lies the submesoscale, which feeds off
 32 of the available potential energy (APE) in the mesoscale fronts, particularly in the mixed layer
 33 (*Boccaletti et al.*, 2007).

34 A number of recent observational and modeling papers have demonstrated a pronounced
 35 seasonality in surface EKE in the submesoscale range, roughly 10-100 km (*Mensa et al.*, 2013;
 36 *Qiu et al.*, 2014; *Sasaki et al.*, 2014; *Callies et al.*, 2015; *Brannigan et al.*, 2015; *Rocha et al.*,
 37 2016b; *Buckingham et al.*, 2016). Most of the studies cited are regional or from idealized
 38 models, thus global patterns have not yet been established. Moreover, there are at least four
 39 main hypotheses proposed to explain this seasonality: (i) variation in internal gravity wave
 40 energy due to seasonality in upper ocean stratification (*Rocha et al.*, 2016b); (ii) variation in
 41 frontogenesis (FG) due to seasonality in lateral strain and convergence in horizontal density
 42 gradients (*Mensa et al.*, 2013); (iii) variation in the interior baroclinic instability (BCI) due
 43 to seasonality in the vertical shear of the full-depth background state (*Qiu et al.*, 2014); and
 44 (iv) variation in the mixed-layer (ML) BCI due to seasonality in ML stratification, depth and
 45 vertical shear in the mixed layer (*Boccaletti et al.*, 2007; *Qiu et al.*, 2014; *Callies et al.*, 2016).
 46 There is as yet no strong consensus about the relative roles of these mechanisms on a global
 47 scale.

48 Current generation satellite altimetry products provide global observations of sea surface
 49 height (SSH), and thus geostrophic velocity, but the spread of the tracks and instrument noise
 50 limit the effective resolution to about 100 km (*Xu and Fu*, 2012), which is just sufficient to
 51 see the peak of the mesoscale. The almost-submesoscale-resolving Surface Water Ocean To-
 52 pography (SWOT) satellite (*Fu and Ferrari*, 2008) is expected to launch in 2021, and until
 53 then, investigations of submesoscale and submesoscale-driven seasonality in EKE must rely on
 54 models.

55 In this paper, we investigate seasonal variability of eddy kinetic energy (EKE) in a state-

56 of-the-art global climate model; specifically the 0.1° -resolution configuration of the Parallel
 57 Ocean Program (POP) model, run within the fully-coupled Community Earth System Model
 58 (CESM) simulation described in *Small et al.* (2014). To our knowledge, the seasonality of
 59 ocean turbulence has not been examined in a coupled model on a global scale. According
 60 to the criteria of *Hallberg* (2013), this configuration ranges from mesoscale-resolving at low
 61 latitudes to mesoscale-permitting at high latitudes. Although this is very fine resolution for a
 62 climate model — finer than resolved by current generation altimeters — it is coarse compared
 63 to recent numerical studies of submesoscale seasonality, some of which have used a spatial
 64 resolution of 1 km or even higher (*Mensa et al.*, 2013; *Sasaki et al.*, 2014; *Gula et al.*, 2014;
 65 *Brannigan et al.*, 2015; *Rocha et al.*, 2016a,b). The lack of resolution is a necessary trade-off
 66 for a global analysis. Moreover, analysis of such a model should provide a useful test bed for
 67 future work on SWOT observations.

68 Driven by this connection to altimetric observations, we focus on the analysis of surface
 69 fields, especially on wavenumber power spectra, which provide a practical way to characterize
 70 scale-dependent variance and have been widely used in related studies (e.g. *Stammer*, 1997;
 71 *Thomas et al.*, 2008; *Capet et al.*, 2008b; *Xu and Fu*, 2011, 2012). An oft-cited motivation for
 72 spectral analysis is its connection to inertial-range turbulence theories, which provide specific
 73 predictions for spectral power law scalings that vary with the nature of the turbulence, suggest-
 74 ing a tempting way to test ideas. For example, *Xu and Fu* (2012) made a global estimate of
 75 two-dimensional (2D) along-track spectral slopes of SSH observed by satellite altimeters on
 76 *Jason-1* and *Jason-2*. They found that in regions of high eddy activity, the SSH spectral slopes
 77 had values between k^{-5} and $k^{-11/3}$, which are consistent with predictions by QG (*Charney*,
 78 1971) and surface-QG (SQG) theory (*Blumen*, 1978; *Held et al.*, 1995; *Lapeyre and Klein*,
 79 2006), respectively. However, such theories formally only apply to scales that are neither di-
 80 rectly forced nor dissipated, are stationary in time, and reflect only one underlying dynamics.
 81 *Callies et al.* (2016) points out that the submesoscale range is likely directly forced, violating
 82 the inertial assumption, and *Dufau et al.* (2016) argues that previous estimates of spectral slopes
 83 from altimetry which do not properly account for the spatial and temporal variability of signif-
 84 icant wave height (e.g. *Xu and Fu*, 2012) may be contaminated by observational noise even in

85 the mesoscale range. Moreover, the very temporal variability we seek to study implies tempo-
 86 ral non-stationarity. Consequently, our study does not emphasize specific values of the spectral
 87 slopes; rather, we simply use spectra as one of many tools to characterize energy variations in
 88 a scale-dependent way.

89 Despite the limitations imposed by the model resolution and strong damping due to dissipa-
 90 tion, we show that the POP simulation resolves some submesoscale generated energy cascading
 91 up to the mesoscale. Moreover, many lines of evidence — including linear stability analysis,
 92 predictions for energy transfer rates, and phase correlations — point to an inverse cascade of
 93 submesoscale energy generation by mixed-layer instability as the primary driver of this season-
 94 ality.

95 The paper is organized as follows. In section 2, we give a brief description of the POP
 96 model. The results of spectral analysis and comparison of the spectral slopes among seasons
 97 are shown in section 3. In section 4 we discuss baroclinic instability at the mesoscale and
 98 submesoscale, and detail our evidence for MLI as a main source of seasonality in EKE. In
 99 section 5, we examine two other possible drivers of seasonality in small-scale EKE: intertia-
 100 gravity waves and frontogenesis. We summarize and conclude in section 6. The details of our
 101 spectral analysis and linear stability analysis are given in the appendix.

102 2 . Description of the numerical model

103 The ocean simulation we examine is a part of the fully-coupled global simulation using the
 104 CESM described in *Small et al.* (2014), which was run under present-day greenhouse gas condi-
 105 tions for 100 years, similar to *McClean et al.* (2011). The POP model, which is the ocean com-
 106 ponent, is a level-coordinate ocean general circulation model that solves the three-dimensional
 107 primitive equations for ocean dynamics. The hydrostatic and Boussinesq approximations are
 108 prescribed, and the model employs a B-grid (scalars at cell centers, vectors at cell corners) for
 109 the horizontal discretization scheme. The time discretization scheme uses a three-time-level
 110 second-order-accurate modified leap-frog scheme for stepping forward in time. The diffusive
 111 terms are evaluated using a forward step.

112 Subgrid scale horizontal mixing is parameterized using biharmonic diffusivity and viscos-

113 ity, with the coefficients spatially varying with the equatorial values of $A_H = -3.0 \times 10^9 \text{ m}^4/\text{s}$
 114 and $A_M = -2.7 \times 10^{10} \text{ m}^4/\text{s}$ respectively. The vertical diffusion depends on the K-profile
 115 parameterization (KPP) of *Large et al.* (1994). Further details about the discretization and ad-
 116 vection schemes of the primitive equations and parameterization methods are described in the
 117 Parallel Ocean Program Reference Manual (*Smith et al.*, 2010). The horizontal grid spacing in
 118 the POP simulation is approximately 0.1° in latitude/longitude. Each component of the cou-
 119 pled model exchanges information at different time intervals, with the atmosphere, sea ice, and
 120 land models coupling every time step (15 min), and the ocean every 6 hours. The simulation
 121 outputs at the ocean surface were saved as daily averages, while interior information was saved
 122 as monthly averages. The available model output constrains the scope of our analysis; since the
 123 monthly averaging filters out lots of small-scale variance, we focus our spectral analysis at the
 124 surface. More details of the model setup can be found in *Small et al.* (2014).

125 A video of the sea surface temperature in the Kuroshio region is available online at <https://vimeo.com/channels/oceandynamics/99933667>. This video clearly shows the
 126 formation of secondary instabilities on the fronts of mesoscale eddies; this process appears to
 127 be much more active in winter, when mixed layers are deep. Although the spatial resolution
 128 of this model (0.1°) is not considered submesoscale resolving, the video suggests that some
 129 submesoscale processes are captured by the model. This visualization provided the motivation
 130 for our subsequent quantitative analysis of seasonality.

132 3 . Spectral Analysis of the Velocity and Tracer Fields

133 Spectral analysis provides a practical way to characterize the scale-dependent variance in
 134 the simulation. To resolve regional variability, we split up the domain over the globe into
 135 10° latitude-longitude boxes and calculate the spectra for each subdomain. For every daily-
 136 averaged field in each subdomain, we remove the spatial mean by subtracting the bi-linear trend
 137 derived from the least-square plane fit of the horizontal fields and apply a 2D Hanning window.
 138 In deriving the wavenumber spectrum, we approximate a local tangent plane in Cartesian ge-
 139 ometry and take the 2D Fourier transform of the anomaly fields. We then take the average over
 140 the azimuthal direction to create an isotropic spectrum. We sample the spatial fields every 13

141 days, which is approximately the temporal decorrelation time. For the purposes of calculating
 142 the error, each individual spectrum is therefore treated as an independent realization of the pro-
 143 cess. Using 41 years of data, we have 1135 individual spectra. Numerical implementation and
 144 normalization of the spectra is discussed in the Appendix A3.

145 *3 .1. Snapshots of tracer fields and example of spectra*

146 The annual mean spectral slopes are shown in Fig. 1 (see Sec. 3 .2 for description of how
 147 slopes are fit). In most regions, the spectral slopes are in the range predicted by QG theory but
 148 some regions have slopes steeper than -3, which is likely due to the presence of dissipation.
 149 Before examining the seasonal variability of this global map, we first examine the details of
 150 the spatial and spectral fields in a few energetic regions of the ocean (Kuroshio, Gulf Stream,
 151 and ACC). The location of the regions is shown in Fig. 1. (Additional regions are presented in
 152 Appendix A.1).

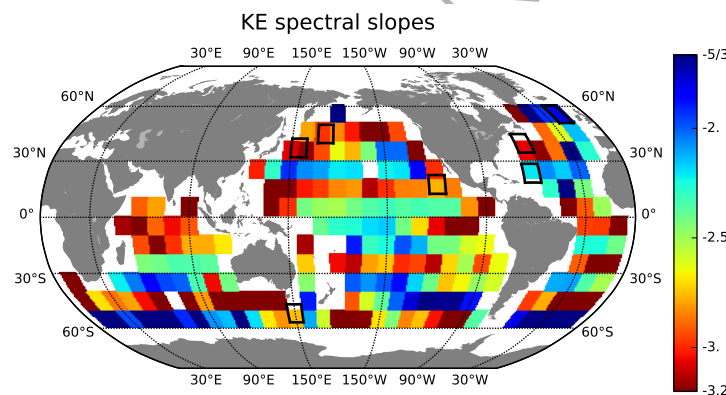


Figure 1: Annual mean of spectral slopes at scales above 200-250km (4×10^{-3} - 5×10^{-3} cpkm). The black boxes indicate the seven regions (Kuroshio, north of Kuroshio, east Pacific, Gulf Stream, Sargasso Sea, northeast Atlantic and the ACC) we consider in detail.

153 Fig. 2 shows instantaneous spatially detrended fields of relative vorticity (ζ) and buoyancy
 154 ($b = -g\delta\rho/\rho_0$; $\delta\rho = \rho - \rho_0$, $\rho_0 \equiv 1025 \text{ kg/m}^3$) on March 1 and September 1 (representative
 155 of winter and summer in the northern hemisphere and visa versa in the southern hemisphere)
 156 in model year 46. We see the spatial fields have more small scale features and sharper fronts on
 157 March 1 in the Kuroshio region and September 1 in the ACC region, particularly in the vorticity
 158 field.

159 Fig. 3 (a–c) shows the seasonally-averaged isotropic wavenumber spectra of EKE for the

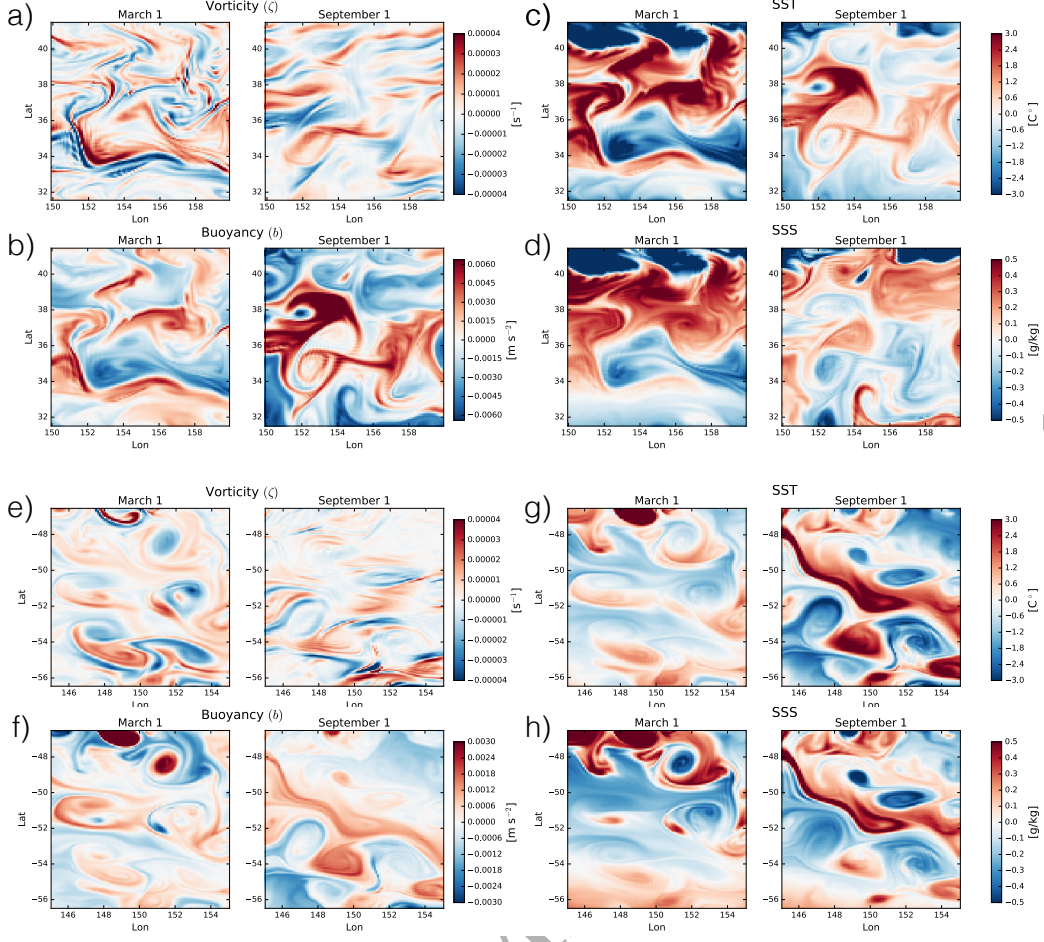


Figure 2: Snapshot of the anomaly fields of vorticity (ζ), buoyancy (b), SST and SSS on March 1 and September 1. The upper panels (a, b, c and d) correspond to the Kuroshio region (lon: 150.0E~160.0E, lat: 31.5N~41.5N) and the lower panels (e, f, g and h) to the ACC region (lon: 145.0E~155.0E, lat: 56.5S~46.5S).

160 Kuroshio, Gulf Stream and ACC regions.

161 Boreal winter is defined as January, February and March (JFM), spring as April, May and
 162 June (AMJ), summer as July, August and September (JAS) and autumn as October, November
 163 and December (OND). (The spectra for the other four regions are shown in Appendix A.1.)
 164 Comparing the EKE spectra for each season, the spring spectra have the highest energy in the
 165 lower mesoscale range (between 50km and 100km, i.e. $10^{-2} - 2 \times 10^{-2}$ cpkm) while autumn
 166 has the lowest energy. At the smallest scales, the EKE spectra have most power in winter and
 167 least power in summer. (Buoyancy spectra are presented and discussed in Sec. 3 .3.)

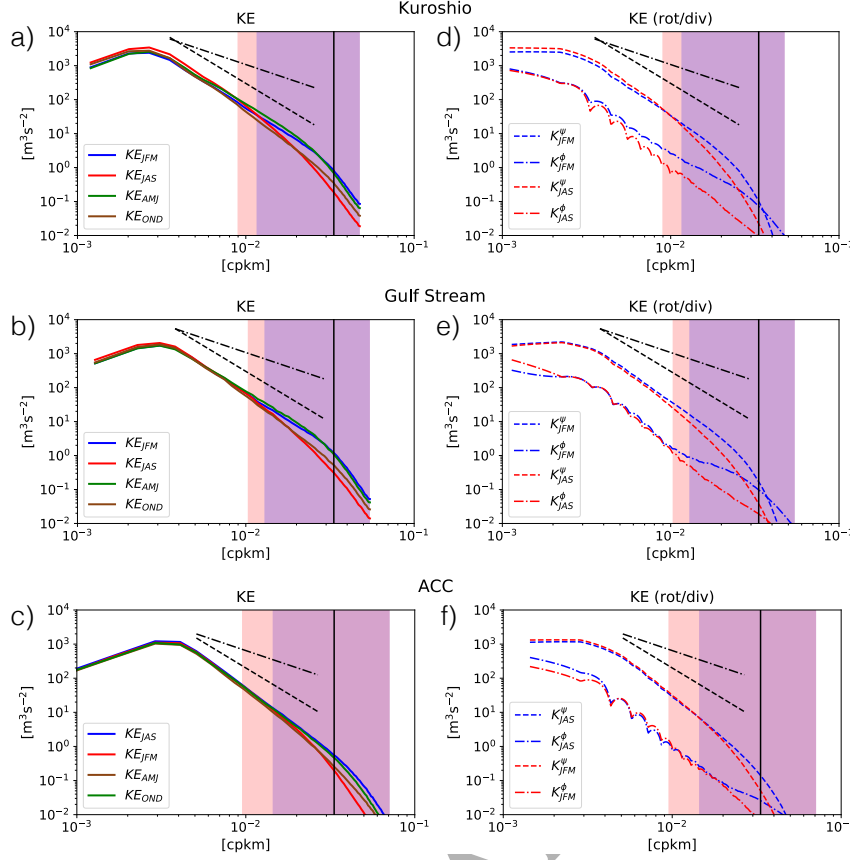


Figure 3: Seasonally-averaged EKE spectra in eddy active regions: (a) Kuroshio, (b) Gulf Stream, and (c) ACC in Fig. 1. The shading shows the dissipation range defined as where 80% of the dissipation due to bihamonic diffusion occurs (blue: winter, red: summer). The black dashed and dotted lines show the spectral slope of -3 and -5/3 respectively. The black vertical line indicates the 30 km scale. The dashed and dotted spectra in panels (d), (e) and (f) show the rotational and divergent component of EKE respectively for each of these regions. The 95% confidence intervals were thinner than the lines used to plot the spectra and so are not shown.

168 3 .2. Seasonal variations kinetic energy spectra

169 Theoretical models of ocean mesoscale turbulence predict spectral slopes in the inertial
 170 range (Charney, 1971; Held *et al.*, 1995) and many previous studies have used spectral slopes
 171 to characterize ocean turbulence in observations and numerical models (e.g. Stammer, 1997;
 172 Capet *et al.*, 2008b; Xu and Fu, 2011, 2012). As pointed out by Callies *et al.* (2016), however,
 173 the actual values of spectral slopes are not dynamically unique and inertial range theories are
 174 invalid at scales that are directly forced. Furthermore, given the strong role of dissipation
 175 and the relatively small wavenumber range resolved by our model, it is unlikely that inertial
 176 range theories apply quantitatively to this simulation. Consequently, we focus on the seasonal
 177 changes in slopes, rather than their absolute values. These slope changes indicate a seasonally

178 varying partition of energy between large and small scales. The slopes were calculated by
 179 fitting a straight line to the log-log spectrum using the least-square method. Due to limited
 180 spatial resolution and the influence of sub-grid dissipation, the slope fit is very sensitive to
 181 the choice of wavenumber range. In addition to dissipating EKE at each scale, the numerical
 182 dissipation also removes EKE due to baroclinic instability that would have otherwise cascaded
 183 upscale, so the spectral slopes are expected to be steeper than predicted by QG turbulence
 184 theories.

185 We address dissipation by explicitly calculating the momentum tendency due to lateral
 186 biharmonic viscosity in the spectral domain (see Appendix A.4 for details). We define the
 187 “dissipation range” as the wavenumber range above which 80% of dissipation occurs. From
 188 Fig. 3, we see that the dissipation range is broad and extends up to 100km. This is likely
 189 the main cause for the relatively steeper spectral slopes at high wavenumbers. The influence
 190 of dissipation means it is problematic to compare the actual values of slopes in this range and
 191 possibly below with turbulent inertial range theory. The dissipation is broad-band so the inertial
 192 range is very narrow, if it exists at all. The seasonal variability could also violate the stationarity
 193 requirement for such a range to exist. The slope fit is, therefore, performed on scales between
 194 200 km and 250 km (i.e. $4 \times 10^{-3} - 5 \times 10^{-3}$ cpkm), which is outside of the dissipation range
 195 globally. Figure 4 shows the resulting slope difference between winter and summer. We see
 196 the seasonal contrast between winter (JFM) and summer (JAS), which is consistent with the
 197 regional spectra (Fig. 3).

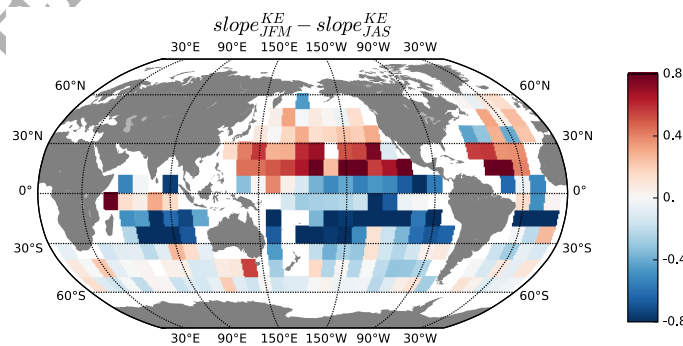


Figure 4: Difference of spectral slopes of EKE between JFM and JAS at scales between 200 km and 250 km (i.e. $4 \times 10^{-3} - 5 \times 10^{-3}$ cpkm).

198 The slope analysis neglects the broad dissipation range, but the strongest variations in spec-

199 tral energy occur within the dissipation range. To quantify the energy at the smallest scales, we
 200 perform a high pass in the spectral range representing scales below 30km (3.3×10^{-2} cpkm);
 201 the resulting seasonal difference in small scale EKE is shown in Fig. 5. A strong seasonal cycle
 202 in is clearly present in both hemispheres. As visible in Fig. 3 these results are not sensitive to
 203 the specific wavenumber range.

204 Seasonality in submesoscale turbulence has been noted in numerous very-high-resolution
 205 regional simulations (Mensa *et al.*, 2013; Sasaki *et al.*, 2014; Qiu *et al.*, 2014) but not in a
 206 global model with $1/10^\circ$ resolution. In order to estimate the relative validity of the amplitude
 207 of this model's seasonal cycle, we compare the POP model EKE levels with the values found by
 208 Sasaki *et al.* (2014) (Fig. 5 (a) in their paper ¹). Sasaki *et al.* (2014) examined a regional model
 209 of the Kuroshio with the resolution of $1/30^\circ$ in the horizontal and 100 vertical levels, finding
 210 a strong seasonal cycle of submesoscale turbulence driven by mixed-layer instability (MLI).
 211 The domain they analyzed was $148^\circ\text{E}-168^\circ\text{W}, 20^\circ\text{N}-43^\circ\text{N}$; our closest regional $10^\circ \times 10^\circ$ box
 212 is $150^\circ\text{E}-160^\circ\text{E}, 31.5^\circ\text{N}-41.5^\circ\text{N}$. The annual-mean $\text{KE}(k)$ at 10^{-2} cpkm is approximately 120
 213 m^3/s^2 in their model and $50 \text{ m}^3/\text{s}^2$ in ours. (It is not surprising that their spectrum has higher
 214 energy levels since their model has a higher spatial resolution.) Comparing the *ratio* of energy
 215 levels at the scale 3×10^{-2} cpkm between winter and summer, the ratio is around 5 in theirs
 216 and 4 in ours. This comparison suggests that the POP simulation produces seasonal variability
 217 of comparable amplitude to submesoscale resolving models, despite the overall lower energy
 218 level.

219 3 .3. Temperature, Salinity, and Buoyancy Spectra

220 We also calculated seasonal isotropic power spectra for potential sea-surface temperature θ
 221 (SST), sea-surface salinity S (SSS), and sea-surface buoyancy b . The buoyancy is defined as
 222 $b = -g\delta\rho/\rho_0$ where $\delta\rho = \rho - \rho_0$ and ρ is derived using the gsw TEOS-10 package (Mc-
 223 Dougall and Barker, 2011) and $\rho_0 = 1025 \text{ kg/m}^3$. The tracer spectra for the three example
 224 regions are shown in Fig. 6. The spectral slope of buoyancy is generally shallower than that of
 225 KE, a finding consistent with results of Callies *et al.* (2016, c.f. Fig. 10 in their paper), although

¹Keeping in mind that the units in Sasaki *et al.* (2014) are [$\text{cm}^2\text{s}^{-2}(\text{cpkm})^{-1}$], there is a factor of 20π when converting them to [m^3/s^2]

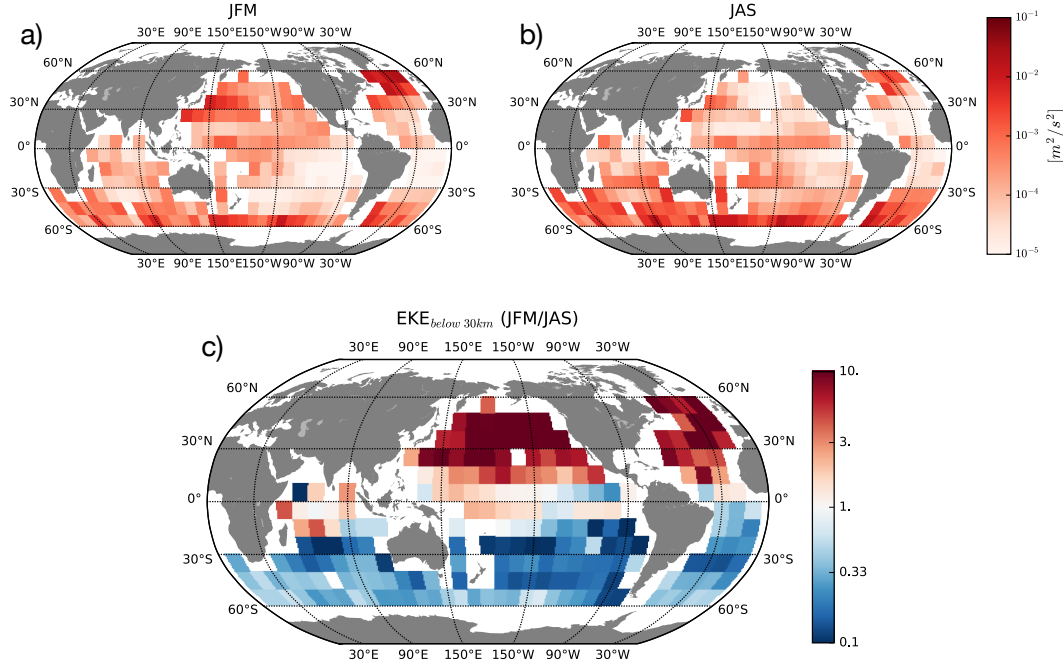


Figure 5: Seasonal climatology of EKE at scales smaller than 30km (3.3×10^{-2} cpkm) for JFM (a), JAS (b) and the ratio between the two (EKE_{JFM}/EKE_{JAS}) (c).

the energy levels themselves are inconsistent with observed *sub-surface buoyancy spectra* (*Cal-lies et al.*, 2015). In contrast to EKE, we do not observe significant seasonal variations in the spectral slope for these tracers. This finding is consistent with the SST spectrum of *Schloesser et al.* (2016, c.f. Fig. 6 in their paper at scales larger than 10km). There is, however, substantial seasonal variability in the overall power level across all length scales.

To examine the seasonality of tracer variance globally, Fig. 7 shows maps of the seasonal difference in small-scale power for buoyancy, SST and SSS between winter and summer. (Since the tracer power level varies uniformly across all analyzed wavenumbers, the choice of averaging band is unimportant here.) The SST power levels show hemispheric seasonality broadly similar to EKE: more SST variance in winter, less in summer. The SSS power levels, in contrast, do not have a coherent hemispheric-scale seasonality, with having opposite seasonality from EKE and SST in some regions. Due to the possibility of compensation between SST and SSS variability, buoyancy variance is not a linear combination of SST and SSS variance. The spatial pattern of seasonal variability of the buoyancy variance (Fig. 7a) more closely resembles the variability of SSS, even at low and mid latitudes. It is likely that a wide range of different processes, especially air-sea interaction, contribute to these patterns of seasonal variability (*F.*

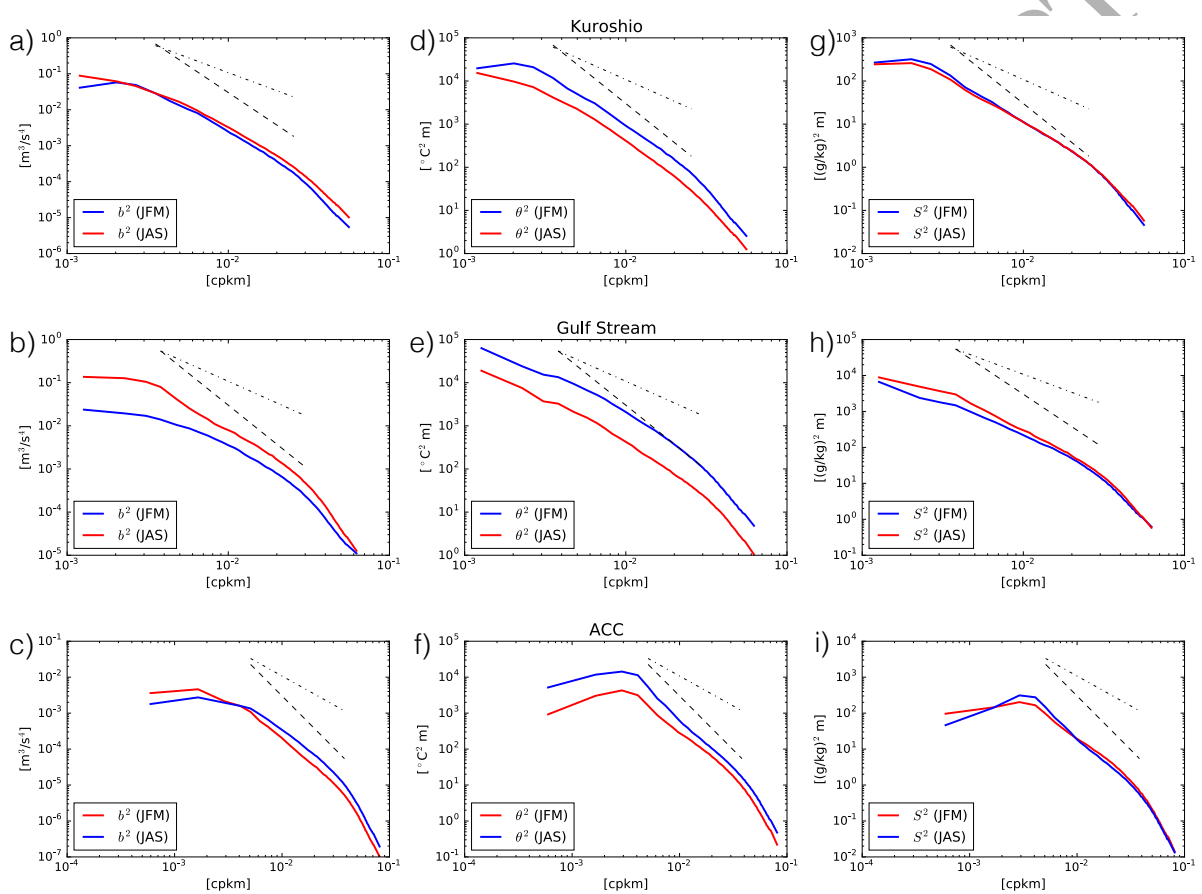


Figure 6: Isotropic wavenumber spectra of buoyancy (a~c), SST (d~f) and SSS (g~i) in the Kuroshio, Gulf Stream and ACC domain in Fig. 1 (blue: winter, red: summer). The black dashed and dotted lines show the spectral slope of -3 and -5/3 respectively.

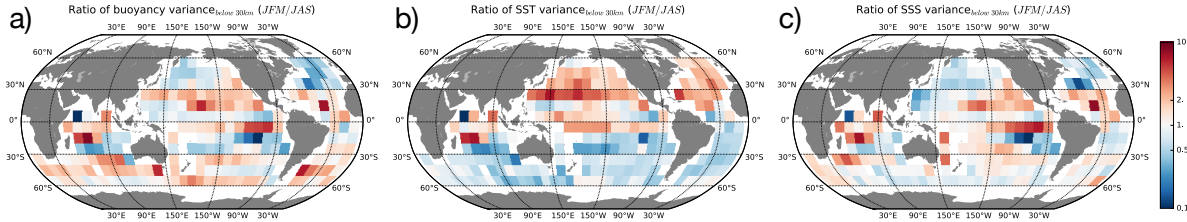


Figure 7: Ratio of tracer variance between JFM and JAS at scales below 30km (i.e. 3.3×10^{-3}) (a) buoyancy, b) SST and c) SSS).

242 Bryan (2017) personal communication).

243 From the buoyancy field, it is tempting to compute surface available potential energy (APE),
 244 especially given its relevance to baroclinic instability (discussed in the next section). Studies
 245 of the energy cycle in global ocean models (e.g. Chen *et al.*, 2016) commonly employ the ap-
 246 proximation $\text{APE} \approx b^2/N^2$, appropriate in a well-stratified incompressible Boussinesq fluid
 247 (e.g. Vallis, 2006). We calculated this quantity in the model mixed layer using daily buoyancy
 248 variance b and a seasonal, 10° -box-averaged climatology of N^2 , but found that the APE level
 249 and its seasonality were completely dominated by the seasonal climatology of the buoyancy
 250 frequency (N^2), with almost no role for the buoyancy variance itself. Upon reflection, this is
 251 unsurprising: the APE approximation used is not suited for weakly-stratified boundary layers,
 252 and even less so in the artificial mixed layer of the POP model, which is set by the K-Profile
 253 Parametrization scheme (Large *et al.*, 1994) and lacks representation of the submesoscale pro-
 254 cesses that act to restratify it in the real ocean.

255 **4 . Evidence for Mixed-Layer Baroclinic Instability as the source for seasonal variations
 256 in EKE**

257 Baroclinic instability (BCI) converts available potential energy (APE) of the background
 258 ocean state into eddy kinetic energy (EKE), generally at or near the scale of the most linearly
 259 unstable mode (Gill *et al.*, 1974). A leading hypothesis for the generation of seasonality in the
 260 submesoscale range is the mixed layer instability (MLI), a form of BCI which extracts potential
 261 energy from buoyancy fronts in the mixed layer (Boccaletti *et al.*, 2007). Since mixed layer
 262 depth and stratification vary substantially over the seasonal cycle, EKE production from MLI
 263 has been shown to be much higher in winter, when mixed layers are deep and stratification
 264 is weak (Callies *et al.*, 2015, 2016). However, seasonal variations in deep BCI, which draws

265 energy from the main thermocline, have also been implicated in driving seasonal variations in
 266 EKE in the North Equatorial Counter Current region (*Qiu et al.*, 2014).

267 MLI occurs on scales near the ML deformation wavelength (L_d^{ML}), which ranges from
 268 several km to less than 1 km (*Boccaletti et al.*, 2007). The study of MLI in numerical models
 269 has consequently mostly focused on models with grid spacing of roughly 4 km or less (e.g.
 270 *Mensa et al.*, 2013; *Sasaki et al.*, 2014; *Qiu et al.*, 2014). The relatively coarse resolution of
 271 the POP simulation, and the large role of dissipation at small scales (as noted in the previous
 272 section), would presumably prevent MLI from emerging. Nevertheless, in this section we show
 273 evidence that the cause of the seasonal variability in EKE described above is indeed MLI.

274 4.1. Baroclinic Conversion Rate

275 BCI produces eddy kinetic energy from potential energy via the vertical eddy flux of buoy-
 276 ancy $\overline{w'b'}$ (*Vallis*, 2006). When high-frequency data is available, this term can be calculated in
 277 the spectral domain, i.e. as the cross spectrum $\Re\{\hat{w}^*\hat{b}\}(k)$, which reveals the spatial scales of
 278 energy production from BCI. This analysis has been used to demonstrate the link between the
 279 scales and growth rates of the most unstable normal modes identified by linear stability analysis
 280 and the finite-amplitude production of kinetic energy in fully developed, nonlinear baroclinic
 281 turbulence (e.g. *Holland*, 1978; *Qiu et al.*, 2014). *Callies et al.* (2016) used such cross spectra
 282 to show the importance of MLI in energizing submesoscale turbulence in idealized QG simu-
 283 lations.

284 In analyzing baroclinic conversion from the POP model, we are somewhat constrained by
 285 the available output. High frequency (daily) data were only saved for the surface, precluding a
 286 spectral decomposition of w and b in the interior. Interior fields were saved as monthly averages,
 287 which heavily filters small-scale fluctuations. However, a six year portion of the integration was
 288 conducted in which this monthly-averaged interior data included the vertical tracer fluxes $\overline{w\theta^m}$
 289 and $\overline{wS^m}$, where the m superscript indicates a temporal average over a single month. From this
 290 output, the monthly-averaged buoyancy flux can be calculated as $\overline{wb^m} \approx g(\alpha\overline{w\theta^m} - \beta\overline{wS^m})$
 291 where α is the thermal expansion and β the haline contraction coefficient determined from the
 292 seasonal climatologies for each 1° grid box.

293 To isolate the baroclinic conversion associated with small-scale motions, we calculate the

294 *sub-monthly* contribution to the vertical buoyancy flux. The sub-monthly fluctuations are de-
 295 fined as anomalies from the instantaneous monthly average (*not* the climatology) and denoted
 296 with a double prime: e.g. $u'' \equiv u - \bar{u}^m$. This temporal high-pass filter acts as a crude spatial
 297 high-pass filter. We tested the effect of this filtering on the surface horizontal velocity fields,
 298 for which daily data is available, and found that it strongly attenuates the EKE spectrum at
 299 wavenumbers less than 5×10^{-3} cpkm while leaving the smaller scales mostly unchanged.
 300 (See Appendix A.3 for discussion and figure.) This filtering thus allows us to focus on baro-
 301 clinic conversion in the high wavenumber range where we observe the strongest seasonality in
 302 EKE.

303 Although we can't directly calculate w'' (or its spectrum) from the available interior output,
 304 we can calculate the sub-monthly vertical buoyancy flux as

$$\overline{w''b''}^m = \overline{wb}^m - \overline{w}^m \overline{b}^m. \quad (1)$$

305 We do this for each month of the six years in which this output is available. The seasonal
 306 climatology of $\overline{w''b''}$ (superscript m dropped because we are dealing with a climatology) is
 307 then calculated by grouping together all the months from each season and averaging over the
 308 upper 100 m of the water column. (Results are not highly sensitive to averaging depth.)

309 The results of this analysis for JFM and JAS are shown in Fig. 8, together with the sea-
 310 sonal difference. The climatologies show that $\overline{w''b''}$ is positive nearly everywhere, indicating
 311 conversion of potential energy to kinetic energy, as expected in MLI and BCI in general. The
 312 conversion is strongest in energetic regions such as the Gulf Stream, Kuroshio, Agulhas, ACC,
 313 and Leeuwin current. The strong seasonal cycle is readily visible by comparing the two seasons
 314 and emerges clearly in the difference plot. The winter hemisphere experiences much stronger
 315 conversion rates, up to 10 times larger than the summer conversion rate.

316 The maximum magnitude of $\overline{w''b''}$ in energetic regions is approximately $10^{-7} \text{ m}^2 \text{ s}^{-3}$, which
 317 is also roughly the amplitude of the seasonal cycle. In comparison, Sasaki *et al.* (2014, Fig. 4b)
 318 diagnosed a seasonal amplitude in baroclinic conversion of approximately $10^{-6} \text{ m}^2 \text{ s}^{-3}$ in a
 319 much higher resolution regional model of the Kuroshio. Brannigan *et al.* (2015, Fig. 19b) found
 320 a seasonal cycle amplitude of approximately $10^{-8} \text{ m}^2 \text{ s}^{-3}$ in an idealized model based on the

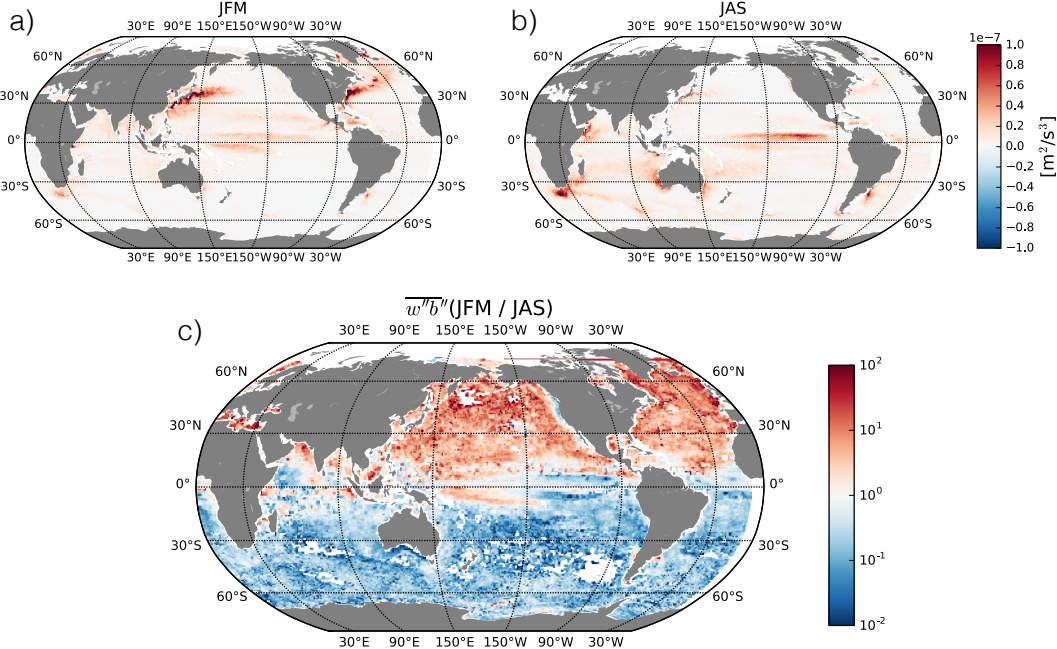


Figure 8: Seasonal climatology of sub-monthly APE conversion rate ($w''b''$) for JFM (a), JAS (b) and the ratio between the two (c).

mid-latitude open ocean run at 0.5 km resolution. These comparison show that the magnitude and seasonal cycle of $\overline{w''b''}$ in the POP model is consistent with, but somewhat weaker than, higher resolution studies of seasonal MLI in eddy active regions.

We also compare the diagnosed $\overline{w''b''}$ with an estimate given by the the MLI parametrization of *Fox-Kemper et al.* (2008), which is based on an Eady-type model of BCI within the mixed layer (see Sec. 4 .2 for further discussion of this model). The parameterization assumes that APE stored in mixed layer fronts is converted to EKE at the rate

$$\overline{w'b'}^{FK} = \frac{\overline{M^4 H^2}}{|f|} \quad (2)$$

where M^4 is the squared horizontal buoyancy gradient, defined as

$$M^4 \equiv \left(\frac{\partial \bar{b}^{xy}}{\partial x} \right)^2 + \left(\frac{\partial \bar{b}^{xy}}{\partial y} \right)^2, \quad (3)$$

H is the mean mixed-layer depth, and f is the Coriolis parameter. This parameterization was designed to be applied to the mesoscale buoyancy gradients, so we first average the buoyancy field horizontally over ten grid points (roughly 1 degree), as indicated by the symbol \bar{b}^{xy} . We

332 then square the gradients of this coarse-grained buoyancy field and finally take the climato-
 333 logical average over seasons (indicated by the overbar in eq. (2)). Since daily-resolution of
 334 buoyancy was only available at the surface, we assume that M^4 is uniform over the mixed
 335 layer.

336 One caveat is that the exact magnitude of the FK-parameterized conversion rate is uncertain
 337 up to a scaling factor and the magnitude of buoyancy gradient in eq. (2) is highly sensitive to
 338 the choice of averaging scale used to define M^4 . Here we choose a scale representative of
 339 the mesoscale fronts which drive MLI. We also focus on the magnitude of the seasonal cycle,
 340 which the scaling factor cancels out and is less sensitive to the choice of averaging scale than
 341 the absolute value of the estimated conversion rate.

342 The JFM and JAS values of $\overline{w'b'}^{FK}$ are shown in Fig. 9. The predicted amplitude of the
 343 seasonal cycle is $10^{-7} \text{ m}^2 \text{ s}^{-3}$, comparable to the diagnosed values. However, the spatial pattern
 344 is somewhat different; while the diagnosed $\overline{w''b''}$ has clear maxima in western boundary cur-
 345 rents, $\overline{w'b'}^{FK}$ is distributed more evenly over the open subtropical oceans. The spatial pattern
 346 of seasonal difference, however, is more similar to that of $\overline{w''b''}$. Given the relatively coarse
 347 resolution of the POP model, and the approximate nature of the the Fox-Kemper parameteriza-
 348 tion, the consistency between the two supports the notion that MLI is the driver of the seasonal
 349 variations in baroclinic conversion and EKE.

350 Finally, we compare $\overline{w''b''}$ with small-scale (below 30km) EKE at monthly resolution from
 351 the three example regions in Fig. 10. The two signals are highly correlated. There is some
 352 indication that the EKE lags the conversion rate by one month. This in-phase relationship
 353 suggests that seasonal changes in $\overline{w''b''}$ equilibrate quickly and are likely balanced on a month-
 354 by-month basis by changes in dissipation and / or spectral energy transfer to larger scales.

355 4.2. Linear Stability Analysis

356 In the preceding section, we showed that the sub-monthly baroclinic conversion rate is
 357 indicative of seasonally varying MLI. The lack of daily output of the interior fields means
 358 that we cannot directly calculate the conversion rate in spectral space. However, *Qiu et al.*
 359 (2014) showed that the temporal variations in finite-amplitude baroclinic conversion were well
 360 captured by variations in the linear stability properties of the background ocean state. Here we

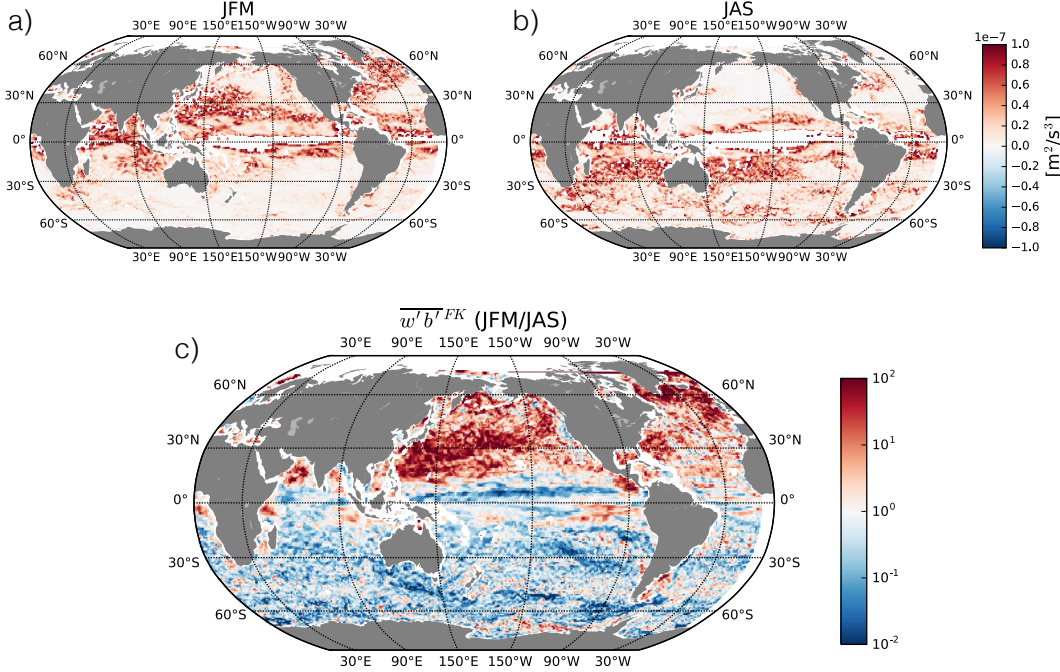


Figure 9: APE conversion rate following the parametrization by Fox-Kemper et al. (2008) ($\overline{w'b}^{FK}$) for JFM (a), JAS (b) and the ratio between the two (c). Values near the equator are masked out for (a) and (b) as the Coriolis parameter becomes small.

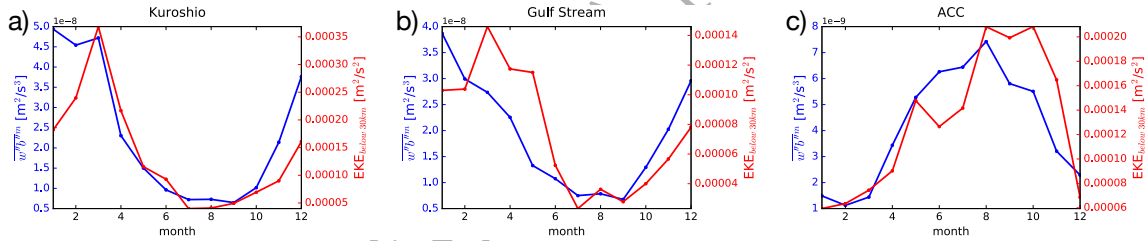


Figure 10: Seasonal phase of $w'b$ and EKE in the Kuroshio (a), Gulf Stream (b) and ACC (c) domain in Fig. 1.

use linear BCI analysis of the POP model climatology to investigate the temporal scales, spatial scales, and the vertical structure of potential instabilities.

We first calculate the growth rates of linear instabilities numerically using the same approach as Smith (2007). This method solves the linear quasigeostrophic (QG) eigenvalue problem using the local profile of geostrophic shear and stratification (N^2) at each point in the horizontal to define the background state. While Smith (2007) considered just the annual mean climatology, here we use a seasonally resolved climatology, revealing how instability varies between winter and summer.

The background state was defined by taking the seasonal climatology over 41 years of model output and aggregating the original 0.1° resolution to 1° . It is instructive to consider

the winter and summer climatological profiles of geostrophic velocity and N^2 , as shown in Fig. 11 (a), an example from the Kuriosio region. While there are some seasonal difference in geostrophic velocity and associated shear, the dominant seasonal change is in the upper ocean N^2 , which is nearly 100 times weaker in the winter profile. This weak winter stratification reflects the cumulative impact of deeper winter mixed layers. The winter N^2 profile can be viewed as a superposition of interannual and intra-seasonal MLD variability over the averaging period. It is, however, problematic to attempt to define an actual mixed-layer depth from the climatological profile; because mixed-layer depth identification (e.g. using a density threshold criterion (*de Boyer Montégut et al.*, 2004)) is a nonlinear operation, the average of the MLD given by the daily resolution output is not the same as the MLD of the climatological density field. For this reason, we define the ML as the depth over which N^2 experiences significant seasonality (approximately 160m in Fig. 11 (a), the depth at which N_{JFM}^2 and N_{JAS}^2 coincide). The ML corresponds roughly with the maximum winter MLD over the averaging interval.

The growth rates of the linear instabilities were determined numerically using the `oceanmodes` python package² developed for this study (hereon we will refer to this as the numerical solution). The numerical details of the linear stability calculation are given in Appendix A.5; here we show only the final results. The growth rates for the same Kuroshio example region are shown in Fig. 11 (c) as a function of zonal wavenumber. (In the example, meridional wavenumber is set to zero, but full two-dimensional stability calculations were also performed.) This figure also shows several relevant length scales: the the full-depth Rossby radius R_d , the mixed-layer (ML) Rossby radius R_d^{ML} , and the model Nyquist wavelength (defined as two grid points $2\Delta x$). R_d was calculated numerically with the `oceanmodes` package using the seasonal climatology of N^2 (buoyancy frequency), while R_d^{ML} was derived from the depth averaged buoyancy frequency over the mixed layer (i.e. $R_d^{ML} = \bar{N}^{z_{ML}} H_{ML}(\pi f)^{-1}$).

We observe large differences between winter and summer numerical growth rates, especially at small scales. A large portion of the small scale instability predicted cannot be resolved by the model, since it occurs at smaller scales than the model grid scale (thick black line in

²This open source package is available at <https://github.com/rabernat/oceanmodes>. Appendix A.5.

398 Fig. 11c). However, there is still a large seasonal difference in the resolved growth rates around
 399 the model Nyquist wavelength and above³. The vertical structure of the mode with a local
 400 maximum growth rate around the Nyquist wavelength, shown in Fig. 11b, is strongly surface
 401 intensified. This is the smallest instability that can potentially be resolved, although its growth
 402 is likely strongly damped by numerical dissipation.

403 To quantify the contribution of the reduced near-surface stratification during winter to the
 404 growth rates, we artificially homogenize the stratification during winter in the ML to the value
 405 at the base of ML and then recalculate the numerical growth rate, leaving the geostrophic
 406 velocity profiles untouched. The blue dotted line in Fig. 11c shows the growth rate (σ_{JFM}^{ML}) for
 407 this modified N^2 profile. We see that the large growth rates at small scales disappear, while the
 408 growth rates near the full-depth deformation radius remain unchanged. This experiment reveals
 409 that the main driver of seasonality in growth rates is indeed the weak near-surface stratification
 410 in winter. Furthermore, the lack of significant seasonal changes in deep shear/stratification and
 411 corresponding large-scale growth rates indicates that deep BCI is unlikely to be the main driver
 412 of seasonality. This general behavior holds for all the seven example regions (not shown).

413 The importance of weak upper ocean stratification in driving seasonality in instability is
 414 consistent with the MLI mechanism (Boccaletti *et al.*, 2007; Callies *et al.*, 2015, 2016). To
 415 test the quantitative connection to MLI theory, we compare the full growth rates to the approx-
 416 imated baroclinic instability models of Eady (1949) (Fig. 11c), which is considered to be a
 417 good approximation for MLI (Boccaletti *et al.*, 2007; Callies *et al.*, 2016). The analytical Eady
 418 growth rates were calculated using the two different assumptions for the Rossby deformation

³Within the ML, the background state of shear and stratification is ill-determined. This limits our interpretation of the actual values of the growth rates but our point shown below is that the large seasonal difference is due to the reduced ML stratification during winter time.

radius: full depth and ML⁴. We find that the ML Eady growth rates during winter are a good proxy for the full numerical solution in the Kuroshio region, capturing roughly the scale and magnitude of the dominant peak (although the numerical solutions contain even smaller-scale instabilities)⁵ Since the ML depth is related to the maximum winter ML depth, it is not surprising that the ML Eady and ML Rossby wavelength $L_d^{ML} (\equiv 2\pi R_d^{ML})$ capture the scales and large growth rates of this mode of instability. Examination of all seven example regions revealed that the ML Eady model qualitatively captures the dominant mode of baroclinic instability around the Nyquist wavelength during winter in eddy active regions (not shown).

We now assess the seasonality in linear instability at the global scale. In Fig. 12, we show the seasonal difference of the maximum numerical growth rates at the Nyquist wavelength (σ_N). (The maximum was taken from the two-dimensional zonal/meridional-wavenumber space.) We see that the maximum growth rates are consistently larger during winter than summer, consistent with the example region examined above and coherent with the seasonal pattern of EKE spectra. It is particularly notable that the reversal of seasonal signals in the tropics of the Pacific Ocean show up both in the EKE and growth rates. The large seasonal difference in growth rates are not just at the Nyquist wavelength but extend to larger scales, as seen in Fig. 11.

If MLI is indeed the driver of the seasonal variations seen in the KE spectra, the unstable mixed-layer modes must be resolved by the model grid. The 0.1° resolution of the POP model is very fine for a climate model, but it is still not even classified as mesoscale resolving at

⁴Due to how the MLD was defined, ML Eady estimates have only been given for winter. The Eady growth rates were defined as

$$\sigma_{Eady} = f_0 \sqrt{\frac{1}{Ri}} \left[\left(\coth \frac{\mu}{2} - \frac{\mu}{2} \right) \left(\frac{\mu}{2} - \tanh \frac{\mu}{2} \right) \right]^{1/2}, \quad k_{max} = 1.6 R_d^{-1}$$

where

$$\sqrt{\frac{1}{Ri}} = \sqrt{\frac{1}{H} \int_{-H}^0 \frac{(\frac{\partial u_g}{\partial z})^2 + (\frac{\partial v_g}{\partial z})^2}{N^2} dz}$$

and H is the full depth or MLD depending on the context.

⁵Unsurprisingly, the (full-depth) Eady solutions using R_d do not provide a very good fit to the numerical solution as it is difficult to assume that the stratification is uniform over the whole depth (Fig. 11 (c)). Henceforth, we will not further consider the full-depth Eady growth rate. Eady (1949) also derived a solution for a model of weak stratification overlying a strong but finite-amplitude thermocline, which was re-examined by Callies *et al.* (2016) in the context of ocean MLI. This idealization is closer to the real ocean where the ML overlies the thermocline, but here we find the ML Eady model to be sufficient.

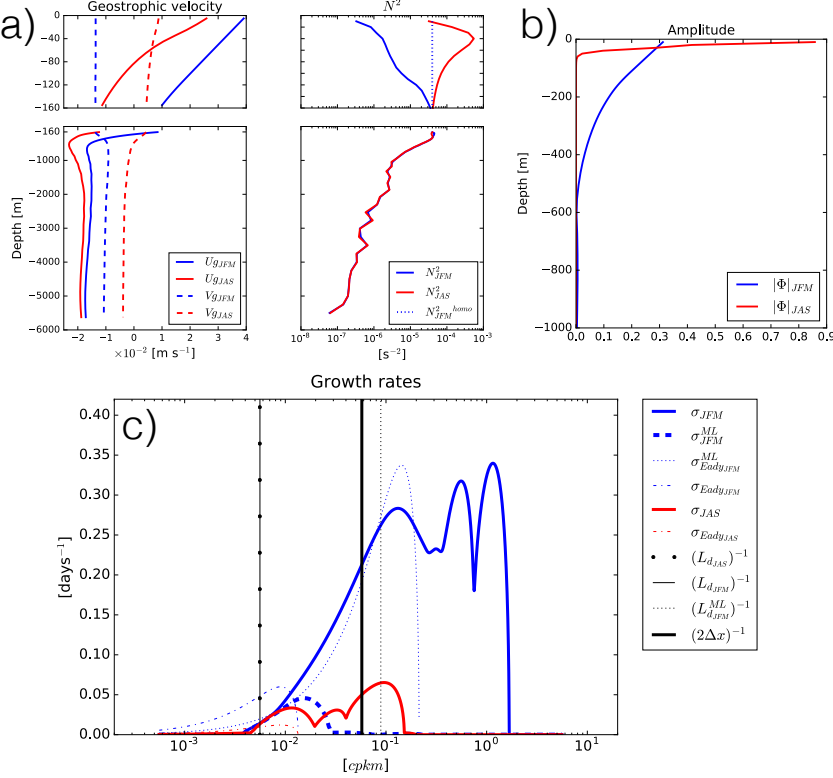


Figure 11: Kuroshio region in Fig. 1 for (a) the geostrophic velocity and buoyancy frequency. We also show the homogenized buoyancy frequency in the ML for winter and summer. The figure is divided at the ML base. (b) Amplitude of the unstable mode with the largest growth rate closest to the Nyquist wavenumber. (c) Numerical solution of growth rates in the Kuroshio region for each season plotted against the zonal inverse wavelength with zero meridional wavenumber: linear instability solved with original profile (solid line) and with homogenized stratification in the ML (dashed line). The Eady (dot-dashed line) and ML Eady (dotted line) growth rate are shown as well. The zonal inverse wavelength was defined between the range of 10^{-1} to $10^3 L_d^{-1}$. The Rossby deformation inverse wavelength are shown in black thin lines and the thick black line indicates the Nyquist wavelength.

high latitudes (Hallberg, 2013)⁶. We argued above that the growth rate at small scales is due to MLI, with a peak at roughly the mixed layer deformation scale L_d^{ML} . The degree to which this is resolved at a particular location depends, then, on how L_d^{ML} varies with grid resolution, or Nyquist wavelength $2\Delta x$. In Fig. 11, we showed that the large growth rates around the Nyquist wavelength are due to the instability around L_d^{ML} where the MLD is defined in the same manner as in Fig. 11. In Fig. 13, we plot the zonal average of L_d and L_d^{ML} , and the ratio of this wavelength to the model Nyquist wavelength in winter and summer. The ratio varies from near 0.1 at low latitudes to 10 at high latitudes. Note also that in Fig. 11, the growth rate

⁶ Note that Hallberg (2013) classifies a model as mesoscale resolving if it resolves the deformation radius R_d of the first internal mode with at least two grid points. The most unstable mode of the linear instability occurs at $L_d^{ML} = 2\pi R_d^{ML} \simeq 6R_d^{ML}$. This is significantly larger than R_d^{ML} itself.

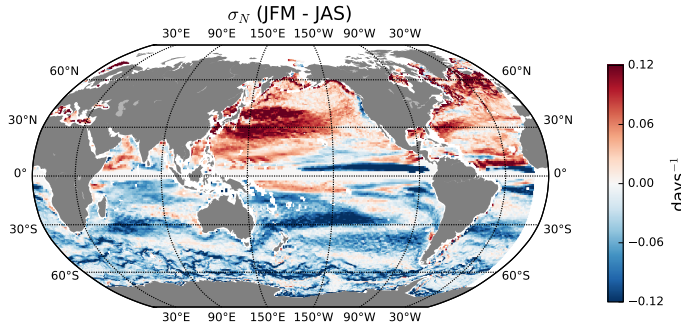


Figure 12: Seasonal difference of the maximum growth rate solved numerically at the Nyquist wavelength.

increases strongly with wavenumber near the model grid scale, implying that, even if L_d^{ML} is not resolved, the fastest-growing resolved instability will still be near the grid scale.

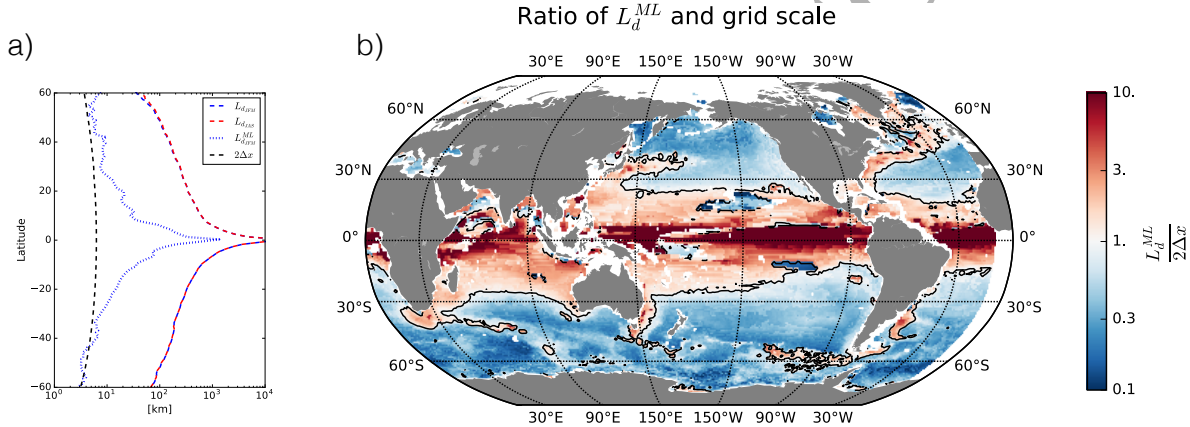


Figure 13: (a) The the zonal average of the Rossby radius (L_d) for winter and summer and the ML Rossy radius (L_d^{ML}) for winter between 60S-60N. The black dashed line indicates the Nyquist wavelength. (b) Ratio of the Rossby wavelength calculated over the mixing layer to the Nyquist wavelength ($L_d^{ML}(2\Delta x)^{-1}$). The values of L_d^{ML} used in the northern hemisphere are values during JFM (boreal winter) and JAS (austral winter) for the southern hemisphere. The black contours indicate where the ratio is unity.

The analysis above shows that there is a strong seasonality in baroclinic conversion rates and growth rates at the Nyquist and larger wavelengths attributable to MLI and partially resolvable by the model. To test the connection between the seasonality in the EKE spectra and MLI globally, we now examine the correlation between the seasonal amplitude in EKE at scales below 30km and $\overline{w''b''}$, the numerical growth rate at the Nyquist wavelength (σ_N) and $\overline{w''b''}$, and EKE at scales below 30km and σ_N in Fig. 14. As EKE and $\overline{w''b''}$ are directly related via the energy budget, it is not surprising that they show the highest correlation ($r = 0.72$; Fig. 14a). EKE was taken at the surface (due to model output availability) while as $\overline{w''b''}$ was

457 taken as the average over the top 100m. Also there is leakage of EKE at scales below 30km due
 458 to nonlinear spectral transfer and dissipation (Arbic *et al.*, 2013, 2014). Given these caveats,
 459 the correlation of 0.72 seems quite high. The correlations with the linear instability growth
 460 rates (Fig. 14b,c) are lower (0.58 for $\overline{w''b''}$ and σ_N ; 0.49 for σ_N and EKE), but still positive.
 461 Processes such as non-linear turbulent interactions and insufficient model resolution towards
 462 higher latitudes (Fig. 13) could be the cause of the lower correlation with the linear instability
 463 growth rate. Nevertheless, these correlations further support the hypothesis that the seasonality
 464 seen in Fig. 4 and 5 is due to MLI.

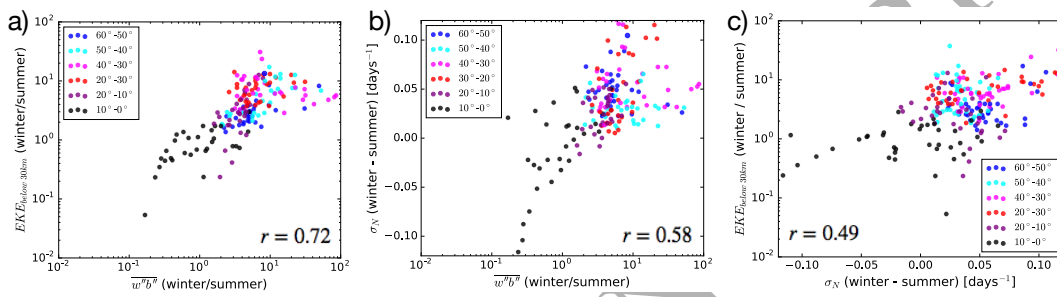


Figure 14: Scatter plot of seasonal difference of (a) EKE against $\overline{w''b''}$, (b) σ_N against $\overline{w''b''}$ and (c) EKE against σ_N . Negative values of $\overline{w''b''}$ were masked out before calculating the correlation. The colors represent each latitudinal band and the correlation coefficient (r) is calculated for the globe.

465 4 .3. Timescale of EKE inverse cascade

466 The EKE spectra (Fig. 3) also show weak seasonal variations at larger scales. The energy
 467 in the smallest scales peaks in winter, while the energy in the larger mesoscale range (between
 468 50km and 100km, i.e. $10^{-2} - 2 \times 10^{-2}$ cpkm) peaks in spring. Sasaki *et al.* (2014) and Qiu
 469 *et al.* (2014) argued that seasonality in submesoscale energy cascades upscale, with a time lag,
 470 to induce seasonality in the mesoscale. In this mechanism, during winter time, deeper ML
 471 and reduced stratification lead to enhanced MLI (Boccaletti *et al.*, 2007; Fox-Kemper *et al.*,
 472 2008), which becomes an energy source during wintertime at the smallest scales. This excess
 473 energy cascades inversely and reaches the mesoscale in the springtime. The inverse cascade of
 474 geostrophic KE was shown extensively by Arbic *et al.* (2013, 2014) to be a robust phenomena
 475 regardless of the spatial resolution even in the presence of dissipation. To test whether this is a
 476 plausible explanation for the POP model mesoscale seasonality, we can quantify the time-lag in
 477 the inverse energy cascade via the eddy turnover timescale. The eddy turnover timescale quan-

478 tifies the rate at which energy is transferred across scales via nonlinear eddy-eddy interaction.

479 It is defined as

$$\tau_k = \frac{k^{-1}}{v_k} = [k^3 \mathcal{E}(k)]^{-1/2} \quad (4)$$

480 (e.g. *Vallis*, 2006) where k , v_k , and $\mathcal{E}(k)$ are the wavenumber, eddy velocity associated the
 481 wavenumber and the EKE spectrum respectively. τ_k can be considered as the approximate timescale
 482 of the spectral energy transfer. As shown in Fig. 15, we obtain values of 40-50 days in the
 483 mesoscale range and 100 days for regions with low eddy activity (not shown). These timescales
 484 are consistent with the mechanism in previous studies (e.g. *Sasaki et al.*, 2014; *Qiu et al.*, 2014)
 485 and suggest that the EKE spectra (Fig. 3) may reflect a time-lagged cascade of submesoscale
 486 energy to larger scales. One caveat is, however, we may be underestimating the “true” values
 487 of \mathcal{E} in the simulation due to the presence of dissipation, and hence overestimating τ_k . As the
 488 temporal and spatial resolution increases, less energy will be dissipated due to dissipation so
 we would expect the real ocean to have smaller τ_k than our estimates.

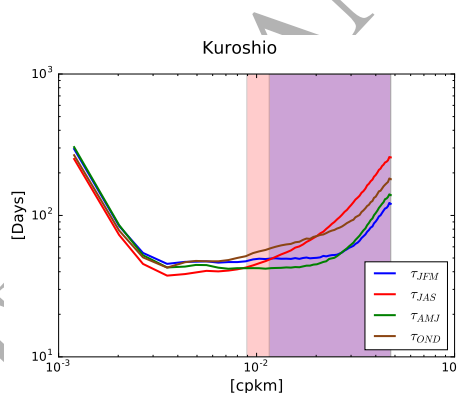


Figure 15: Eddy turnover timescale in days for the Kuroshio region in Fig. 1. The color shadings represent the EKE dissipation range for JFM (blue) and JAS (red).

489

490 **5 . Other Possible Mechanisms for Seasonality in EKE**

491 In this section, we examine alternative possible mechanisms for the generation of seasonal
 492 variability in EKE at and below the 30km scale.

493 *5 .1. Variation in gravity wave energy*

494 In a recent study, *Rocha et al.* (2016b) attribute some seasonality in upper ocean kinetic en-
 495 ergy to inertia-gravity waves, particularly during summer. It is important to note that the POP

496 simulation does not include tidal forcings (*Small et al.*, 2014), so the main mechanism for gen-
 497 eration of super-inertial energy is high-frequency wind forcing. We quantify the contribution of
 498 the inertia-gravity waves by decomposing the horizontal kinetic energy spectra into rotational
 499 (ψ) and divergent (ϕ) components (*Callies and Ferrari*, 2013; *Bühler et al.*, 2014; *Rocha et al.*,
 500 2016a), which assumes isotropy and homogeneity of the field. The decomposed spectra indi-
 501 cates the energy contained in each component (ψ, ϕ) respectively. Internal gravity waves are
 502 divergent by nature in a 2D sense, while balanced flow is non-divergent to leading order, and
 503 so the divergent spectrum approximates the kinetic energy contained in internal gravity waves.

504 We performed this decomposition in the same seven regions where we did the linear sta-
 505 bility analysis. Figure 3 (d~f) and 17 (e~h) show that for all regions, except for the highest
 506 wavenumbers, the rotational component dominates for both seasons. The seasonality seen in
 507 the POP simulation at scales larger than 50km, therefore, is mostly due to the rotational com-
 508 ponent of the velocity field, i.e. geostrophic turbulence, which is non-divergent to first order.
 509 The divergent component at the highest wavenumbers is possibly due to small-scale dissipation
 510 producing significant ageostrophic motion.

511 5.2. Variation in frontogenesis

512 Another proposed mechanism for generating submesoscale energy is frontogenesis (FG)
 513 (*Mensa et al.*, 2013). FG is initiated by mesoscale straining, which sharpens buoyancy fronts.
 514 Below the surface, secondary ageostrophic circulation act to flatten out the isopycnal slopes,
 515 but at the surface, the ageostrophic vertical velocities vanish and the buoyancy fronts sharpen
 516 more rapidly (*Capet et al.*, 2008a). The resulting thermal wind shear leads to sharply surface-
 517 intensified EKE in the submesoscale range.

518 The relevance of strain-induced FG (*McWilliams*, 2016) in producing seasonality at subme-
 519 soscales can be quantified via the frontogenesis function, defined as

$$F_s = \mathbf{Q}_s \cdot \nabla_z b \quad (5)$$

520 where ∇_z is the horizontal gradient and

$$\mathbf{Q}_s = - \left(\frac{\partial u}{\partial x} \frac{\partial b}{\partial x} + \frac{\partial v}{\partial x} \frac{\partial b}{\partial y}, \frac{\partial u}{\partial y} \frac{\partial b}{\partial x} + \frac{\partial v}{\partial y} \frac{\partial b}{\partial y} \right). \quad (6)$$

521 F_s represents the instantaneous rate of increase of the horizontal buoyancy gradient variance
 522 arising from the straining by the horizontal velocity field (*Hoskins*, 1982; *Capet et al.*, 2008a;
 523 *Brannigan et al.*, 2015) (as in *Capet et al.* (2008a) where we neglect the vertical advection
 524 term). Histograms of F_s from different seasons and regions are shown in Fig. 16. The distribu-
 525 tions are strongly skewed toward positive values, which is expected as advective velocities act
 526 to strengthen fronts. Although there is seasonality in the Kuroshio and Gulf Stream region, it is
 527 very weak (the y -axis in the histogram is in log scale). As for the ACC region, the seasonality
 528 is out of phase from that of EKE spectra (Fig. 5), i.e. EKE is higher during JAS (austral winter)
 529 but the frontogenesis function has a longer tail during JFM (austral summer). The other regions
 530 (shown in Appendix A.1) mostly show opposite seasonality from EKE, as in the ACC⁷. This
 531 is consistent with *Brannigan et al.* (2015), who found strong FG in summer/late fall and strong
 532 symmetric instability and MLI in the winter-early spring. Since EKE at scales smaller than
 533 30km has highest levels during winter for both hemispheres, frontogenesis is not likely to be
 534 the cause for the EKE seasonality in the POP simulation.

535 Although FG does not seem to be the dominant factor in causing seasonality in EKE, we
 536 did find that FG is strongest during summertime, consistent with results shown by *Brannigan*
 537 *et al.* (2015). One possible explanation is that the energetic MLI during winter counteracts
 538 FG by slumping the isopycnals, which FG feeds off of and as a result, FG is strongest during
 539 summer when MLI is weak. Since this is the time of year when the MLD is shallowest, FG
 540 may still be an important mechanism for transporting tracers across the ML base and impacting
 541 the biogeochemistry in the surface layer.

⁷The EKE in the tropical Pacific domain had opposite seasonality from the rest of the domain, i.e. higher EKE during summertime, so the seasonality of F_s in the East Pacific domain is out of phase as well.

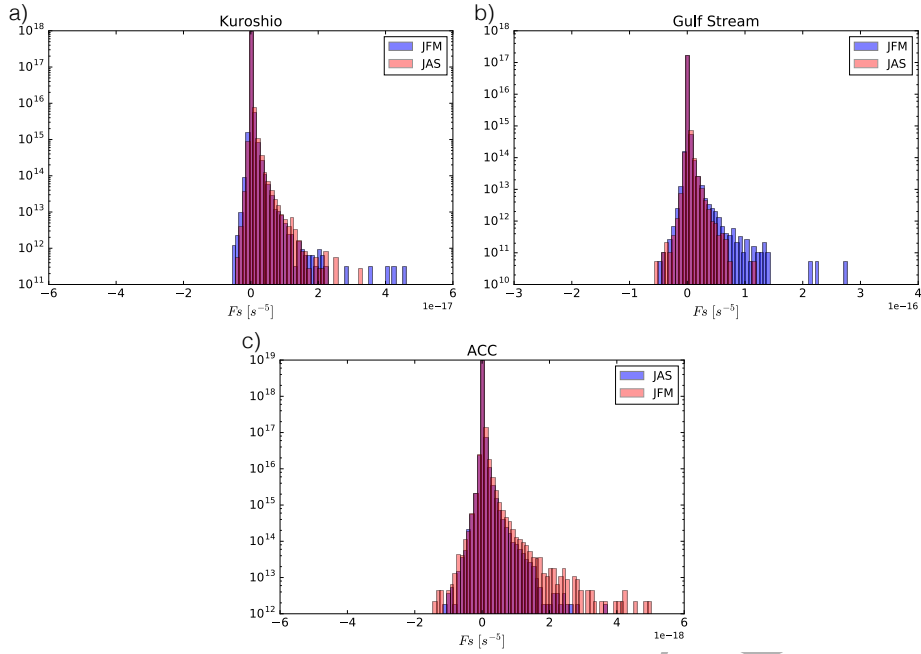


Figure 16: Histogram of the frontogenesis function in the a) Kuroshio, b) Gulf Stream and c) ACC regions shown in Fig. 1. The y -axis is in a log scale to emphasize the seasonality and the histograms are normalized so that the area integrates to unity.

542 6 . Conclusions

543 We have assessed the seasonality in ocean surface eddy kinetic energy in the ocean component
 544 of a global climate model. Although this model is not considered submesoscale-resolving,
 545 our analysis clearly shows significant seasonal differences in both magnitudes and spectral
 546 slopes of wavenumber power spectra of EKE, with a clear signature of seasonally varying
 547 mixed-layer baroclinic instability as its primary driver. This is the central result of our study.

548 In terms of the actual values of the spectral slopes, it was difficult to extract physical mean-
 549 ings and compare them to turbulent inertial range predictions because the subgrid diffusion
 550 impacted the spectra over a wide range of wavenumbers. We therefore calculated the seasonal
 551 difference of spectral slopes at scales between $200 - 250\text{km}$ ($4 \times 10^{-3} - 5 \times 10^{-3} \text{ cpkm}$), while
 552 for the smallest scales (below 30 km), we simply calculated the seasonal different in total en-
 553 ergy and variance. Spring had the shallowest slopes and wintertime had the highest energy at
 554 the smallest scales.

555 As mentioned in the introduction, there have been four major hypotheses proposed in ex-
 556 plaining seasonality in mesoscale turbulence: (i) variation in internal gravity waves due to
 557 seasonality in re-stratification of the upper ocean (Rocha *et al.*, 2016b); (ii) variation in fronto-

genesis due to seasonality in lateral strain and convergence in the horizontal density gradients (Mensa *et al.*, 2013); (iii) variation in the interior baroclinic instability (BCI) due to seasonality in the vertical shear of the full-depth background state (Qiu *et al.*, 2014); and (iv) variation in the mixed-layer BCI (MLI) due to seasonality in ML stratification, depth and vertical shear in the mixed layer (Boccaletti *et al.*, 2007; Qiu *et al.*, 2014; Callies *et al.*, 2016). We have sought to figure out which of these mechanisms, if any, are active in the POP simulation.

We found that the seasonality seen in the EKE field is consistent with observational studies and the predictions of MLI, which can be approximated by the ML Eady model in eddy-active regions (e.g. Callies and Ferrari, 2013; Callies *et al.*, 2015). When the ML depth is deeper during wintertime, available potential energy for BCI increases. This energizes the entire mixed layer and, subsequently, the submesoscale range through non-linear interactions among scales in turbulence (Callies *et al.*, 2015; Brannigan *et al.*, 2015). Since the grid scale of the POP simulation is on the same order of the length scale at which the growth rate of MLI is largest, MLI is at least partially resolved in the POP simulation. Due to the inverse cascade, energy is transported between scales from small to large (Arbic *et al.*, 2013, 2014), which is likely what is seen in the wavenumber spectra. Sasaki *et al.* (2014) and Qiu *et al.* (2014) showed a time-lag in the energy to cascade upscale, and our results are consistent with their finding; winter has the highest energy at the smallest scales, spring and autumn spectra have the highest and lowest energy respectively in the range of 50-100km ($10^{-2} - 5 \times 10^{-2}$ cpkm) and summertime has the highest energy at the largest scales.

The POP simulation has the spatial resolution of 0.1° in latitude and longitude. Due to the subgrid diffusion, however, the effective spatial resolution is much coarser. Consequently, we were very surprised to find evidence of a partially resolved seasonal cycle in MLI. Nevertheless, multiple lines of evidence support the hypothesis of MLI being the dominant cause for seasonality of small-scale EKE in this simulation. There is no such evidence for the other proposed mechanisms we considered (inertia-gravity waves, deep BCI or frontogenesis).

Although there have been numerous studies of MLI in idealized models (Boccaletti *et al.*, 2007; Fox-Kemper *et al.*, 2008; Fox-Kemper and Ferrari, 2008; Brannigan *et al.*, 2015; Callies *et al.*, 2016) and specific regions (Qiu *et al.*, 2014; Callies *et al.*, 2015), this is the first study

describing simulations which resolves the seasonal cycle of MLI on a global scale. It is likely that the MLI in the POP model is severely damped and consequently unrealistic in many respects. Nevertheless, the presence of clear seasonality signals at 30km (3.3×10^{-2} cpkm) and below in every ocean basin implies a robust mechanism for seasonality despite the limited resolution of the model. The implications of this seasonality for air-sea interaction, ocean ecosystems, and eddy fluxes are important questions for future research.

Acknowledgements This research was supported by NASA Award NNX16AJ35G. Abernathey acknowledges additional support from NSF Award OCE-1553593. Uchida acknowledges additional support from the Heiwa Nakajima Foundation. We thank Frank Bryan and Justin Small for sharing the CESM simulation outputs. Data was accessed via the Yellowstone computing system (ark:/85065/d7wd3xhc), provided by NCAR's Computational and Information Systems Laboratory, sponsored by the National Science Foundation. We also thank Jörn Callies and another anonymous reviewer for their constructive feedback.

Appendix

A .1. Isotropic wavenumber spectra and histogram of the frontogenesis function in other regions

Figure 17 shows the isotropic wavenumber spectra of EKE and buoyancy for regions other than the ones shown in Fig. 3 for each season. The EKE spectra is decomposed into the rotational and divergent component.

Figure 18 shows the histogram of the frontogenesis function for winter and summertime for the same region as Fig. 17. We see that the PDFs are strongly skewed towards positive values and that the seasonality is opposite from that of EKE (Fig. 5).

A .2. Sub-monthly spectrum of EKE

We define the sub-monthly velocity anomaly as

$$\mathbf{v}'' = \mathbf{v} - \bar{\mathbf{v}}^m \quad (7)$$

where the superscript m represents the individual monthly mean. The sub-monthly EKE (defined as $EKE'' \equiv 0.5(u'' + v'')$) is show in Fig. 19 for the Kuroshio, Gulf Stream and ACC

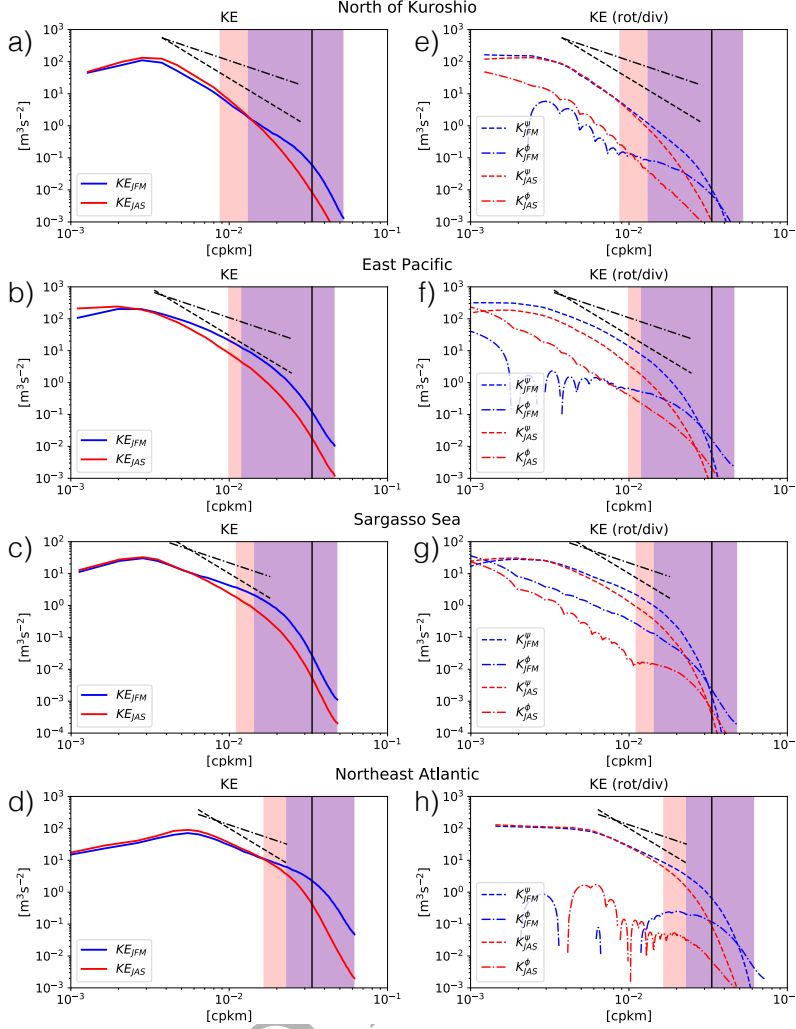


Figure 17: Seasonally-averaged spectra in: (a) north of Kuroshio, (b) east Pacific, (c) Sargasso Sea, and (d) northeast Atlantic. The colored dotted-dashed lines show the EKE'' spectrum derived using the velocity anomaly from the monthly mean. The shading shows the dissipation range defined as where 80% of the dissipation due to bihamonic diffusion occurs and the black dashed and dotted lines show the spectral slope of -3 and -5/3 respectively. Panels (e)~(h) show the rotational and divergent component of the full EKE.

domain. Rest of the domains are shown in Fig. 17. We see that the monthly mean acts virtually as a low-pass spatial filter and the small-scale features are retained in the anomaly field from that.

615 A .3. Method for Calculating Isotropic Spectra

Here we derive the normalization factors related to the calculation of isotropic wavenumber spectra. For an arbitrary 2D scalar quantity $\theta(x, y)$ with units of $[D]$, the corresponding isotropic wavenumber spectrum is denoted as $B(k_r)$, where k_r is the isotropic wavenumber. We wish for $B(k_r)$ to satisfy the Plancherel theorem, such that the total variance is the

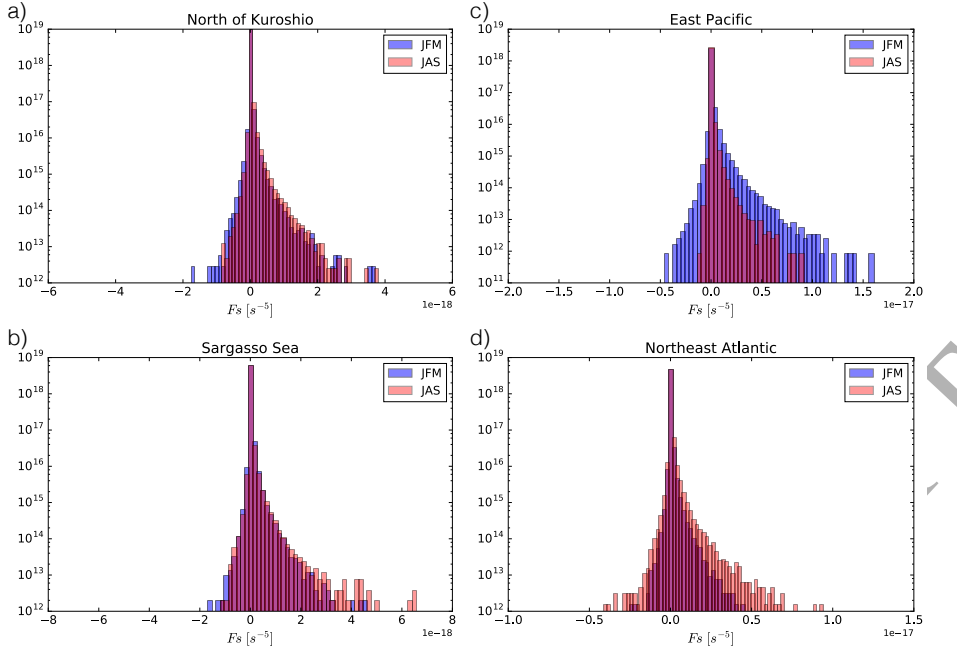


Figure 18: Histogram of the frontogenesis function in the a) North of Kuroshio, b) Sargasso Sea, c) East Pacific and d) Northeast Atlantic regions shown in Fig. 1. The y-axis is in a log scale to emphasize the seasonality.

same when averaged over space or integrated over wavenumber, i.e.

$$\overline{\theta^2}^{xy} = \frac{1}{XY} \int_{-\infty}^{\infty} \int_{-\infty}^{\infty} \theta^2(x, y) dx dy = \int_0^{\infty} B(k_r) dk_r \quad [D^2].$$

the first integral is a spatial average, and the second is a spectral integral. X and Y are the spatial domain lengths respectively.

We now need to relate $B(k_r)$ to quantities we can calculate numerically. For a two-dimensional Fourier transform (FT), the inverse transform is

$$\theta(x, y) = \int_{-\infty}^{\infty} \int_{-\infty}^{\infty} \hat{\theta}(k, l) e^{2\pi i(kx+ly)} dk dl$$

where k and l are zonal and meridional wavenumber. The FT is then

$$\begin{aligned} \hat{\theta}(k, l) &= \int_{-\infty}^{\infty} \int_{-\infty}^{\infty} \theta(x, y) e^{-2\pi i(kx+ly)} dx dy \\ &\approx \Delta x \Delta y \sum_p \sum_q \theta(x_p, y_q) e^{-2\pi i(kx_p+ly_q)} \quad [D m^2] \end{aligned}$$

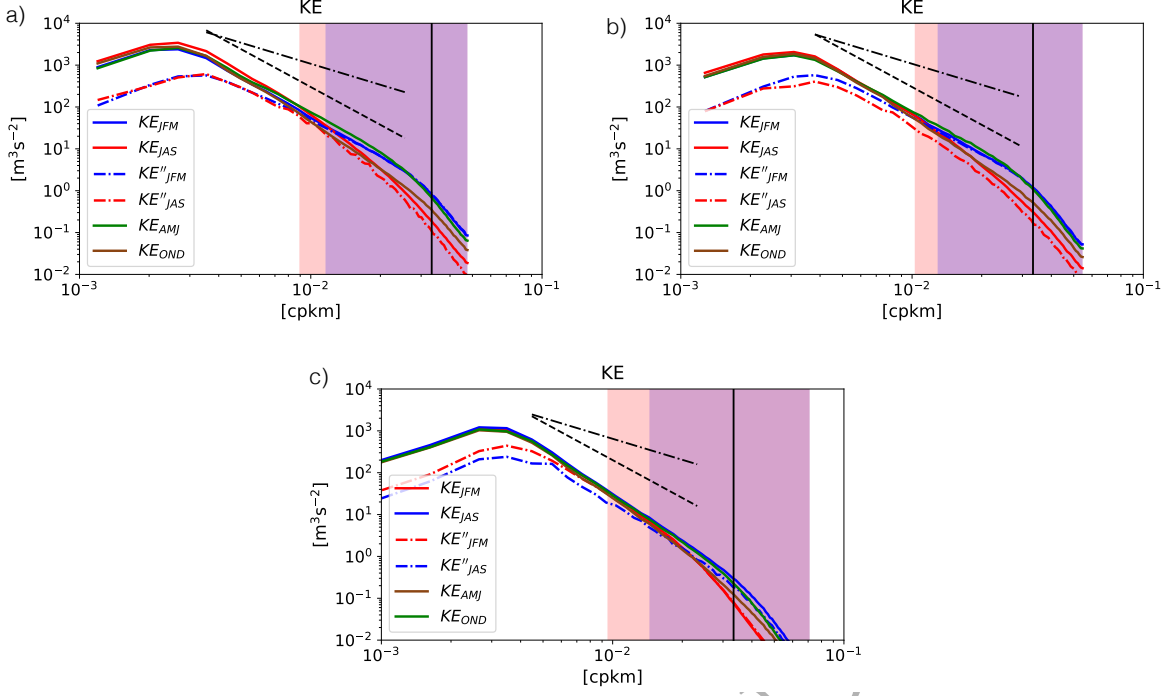


Figure 19: Seasonally-averaged spectra in: (a) Kuroshio, (b) Gulf Stream, and (c) ACC. The colored dotted-dashed lines show the EKE'' spectrum derived using the velocity anomaly from the monthly mean. The shading shows the dissipation range defined as where 80% of the dissipation due to bihamonic diffusion occurs and the black dashed and dotted lines show the spectral slope of -3 and -5/3 respectively.

where the second equality represents the approximation of discretizing the continuous (FT) into a Fourier series. $\hat{\theta}$ has the units of $[D \text{ m}^2]$. Numerical simulations and observations are in most cases discretely sampled data so the discrete FT is necessary. For convenience, we define another variable, indicated by a tilde, for which we absorb the spatial units into the Fourier representation, i.e.

$$\tilde{\theta}(k, l) \equiv \sum_p \sum_q \theta(x_p, y_q) e^{-2\pi i(kx_p + ly_q)}$$

which has the units of $[D]$. The Plancherel theorem in two-dimensions (2D) is

$$\int_{-\infty}^{\infty} \int_{-\infty}^{\infty} \theta(x, y)^2 dx dy = \int_{-\infty}^{\infty} \int_{-\infty}^{\infty} |\hat{\theta}(k, l)|^2 dk dl .$$

Writing out the right-hand side (RHS) in a discrete form, we obtain

$$\begin{aligned}
 \Delta x \Delta y \sum_p \sum_q \theta(x_p, y_q)^2 &\approx \int_{-\infty}^{\infty} \int_{-\infty}^{\infty} \theta(x, y)^2 dx dy \\
 &= \int_{-\infty}^{\infty} \int_{-\infty}^{\infty} |\hat{\theta}(k, l)|^2 dk dl \\
 &\approx \Delta k \Delta l \sum_m \sum_n |\hat{\theta}(k_m, l_n)|^2 \\
 &= \Delta k \Delta l (\Delta x \Delta y)^2 \sum_m \sum_n |\tilde{\theta}(k_m, l_n)|^2 .
 \end{aligned}$$

$\Delta x, \Delta y$ are the spacings between the data points in the spatial domain and $\Delta k, \Delta l$ are the spacings between each discrete inverse wavelength. The discrete inverse wavelengths are defined as

$$k \equiv \frac{(-\frac{N_x}{2}, \dots, -1, 0, 1, \dots, \frac{N_x}{2} - 1)}{N_x \Delta x}, \quad l \equiv \frac{(-\frac{N_y}{2}, \dots, -1, 0, 1, \dots, \frac{N_y}{2} - 1)}{N_y \Delta y}$$

618 where N_x, N_y are the number of data points in the spatial domain.

Hence, the Plancherel relation in the discrete form becomes

$$\Delta x \Delta y \sum_p \sum_q \theta(x_p, y_q)^2 = \frac{1}{N_x^2 N_y^2 \Delta k \Delta l} \sum_m \sum_n |\tilde{\theta}(k_m, l_n)|^2 .$$

619 Now, defining the normalized discrete Fourier coefficients as

$$\check{\theta}(k_m, l_n) \equiv \frac{1}{N_x N_y \sqrt{\Delta k \Delta l}} \tilde{\theta}(k_m, l_n) \quad [D \text{ m}] \quad (\text{A-1})$$

in which $\check{\theta}$ represents the square root of power spectral density (PSD), the discrete Plancherel theorem becomes

$$\Delta x \Delta y \sum_p \sum_q \theta(x_p, y_q)^2 = \sum_m \sum_n |\check{\theta}(k_m, l_n)|^2 .$$

The isotropic PSD, however, needs to be defined carefully. Since it involves a transformation to polar coordinates, we pick up an extra factor of k_r in the integral. In order to satisfy the

Plancherel's relation in 2D, we need

$$\begin{aligned} \int_0^\infty \int_{-\pi}^\pi B(k_r, \phi) d\phi dk_r &= \overline{\theta^2}^{xy} = \int_0^\infty \int_{-\pi}^\pi (|\hat{\theta}(k_r, \phi)|^2 k_r d\phi) dk_r \\ &\approx \frac{1}{\pi R^2} \int_0^R \left(\int_{-\pi}^\pi |\hat{\theta}(k_r, \phi)|^2 k_r d\phi \right) dk_r \quad [D^2] \\ \therefore \int_{-\pi}^\pi B_{2D}(k_r, \phi) d\phi &= \frac{1}{\pi R^2} \int_{-\pi}^\pi |\hat{\theta}(k_r, \phi)|^2 k_r d\phi \quad [D^2m] \end{aligned}$$

620 where $\Delta k_r \equiv \frac{1}{N_r \Delta r}$ and $N_r, \Delta r$ are the number of data points in the radial direction and spacing
621 between the data points respectively.

For an isotropic field, this reduces to

$$\overline{\theta^2}^{xy} = \int_0^\infty B_{2D}(k_r) dk_r \approx \sum_n B_{2D}(k_{rn}) \Delta k_r = (\Delta k_r)^3 \sum_n \frac{k_{rn}}{\pi} |\hat{\theta}(k_{rn})|^2 \quad [D^2] .$$

Using the results above, the relation between the Cartesian and polar coordinate for the Fourier components are

$$\begin{aligned} |\hat{\theta}(k_m, l_n)|^2 &= (N_x \Delta x)(N_y \Delta y) |\check{\theta}(k_m, l_n)|^2 \Leftrightarrow |\hat{\theta}(k_{rn}, \phi)|^2 = \pi (N_r \Delta r)^2 |\check{\theta}(k_{rn}, \phi)|^2 \\ &\Leftrightarrow |\hat{\theta}(k_{rn}, \phi)|^2 = \frac{\pi}{(\Delta k_r)^2} |\check{\theta}(k_{rn}, \phi)|^2 \quad [D^2] . \end{aligned}$$

In an isotropic state

$$|\hat{\theta}(k_{rn})|^2 = \frac{\pi}{(\Delta k_r)^2} |\check{\theta}(k_{rn})|^2 \quad [D^2] .$$

Hence the PSD $B_{2D}(k_r)$ becomes

$$B_{2D}(k_{rn}) = k_{rn} \frac{(\Delta k_r)^2}{\pi} |\hat{\theta}(k_{rn})|^2 = k_{rn} |\check{\theta}(k_{rn})|^2 \quad [D^2m] .$$

622 A .4. Confidence Interval for Spectra

We shall refer to *Menke and Menke* (2009). From the Plancherel theorem, we have

$$\begin{aligned} \Delta x \Delta y \sum_{p=0}^{N_x-1} \sum_{q=0}^{N_y-1} w^{i^2}(x_p, y_q) d^{i^2}(x_p, y_q) &\approx \iint [w(x, y) d(x, y)^i]^2 dx dy \\ &= \iint |\hat{d}^i(k, l)|^2 dk dl \\ &\approx \Delta k \Delta l \sum_{m=-N_x/2+1}^{N_x/2} \sum_{n=-N_y/2+1}^{N_y/2} |\hat{d}^i(k_m, l_n)|^2 \end{aligned}$$

where $w(x, y)$ and $d(x, y)$ are the tapering function and data respectively and \hat{d} includes the tapering. Using the relation shown in the Appendix A3 yields

$$\Delta k \Delta l \sum_m^{N_x/2+1} \sum_n^{N_y/2+1} |\hat{d}^i(k_m, l_n)|^2 = \Delta k \Delta l (\Delta x \Delta y)^2 \sum_{m=-N_x/2+1}^{N_x/2} \sum_{n=-N_y/2+1}^{N_y/2} |\tilde{d}^i(k_m, l_n)|^2$$

so we get

$$\sum_p^{N_x} \sum_q^{N_y} (w^i(x_p, y_q) d^i(x_p, y_q))^2 = \frac{1}{N_x N_y} \sum_{m=-N_x/2+1}^{N_x/2} \sum_{n=-N_y/2+1}^{N_y/2} |\tilde{d}^i(k_m, l_n)|^2 \quad (*) \quad .$$

We can approximate the left-hand side (LHS) of the equation above as

$$\begin{aligned} (N_x N_y) \sum_p^{N_x} \sum_q^{N_y} (w^i(x_p, y_q) d^i(x_p, y_q))^2 &\sim \sum_p^{N_x} \sum_q^{N_y} w_{pq}^{i^2} \sum_p^{N_x} \sum_q^{N_y} d_{pq}^{i^2} \\ &= \frac{1}{N_x N_y} \sum_p^{N_x} \sum_q^{N_y} w_{pq}^{i^2} (N_x N_y)^2 \frac{1}{N_x N_y} \sum_p^{N_x} \sum_q^{N_y} d_{pq}^{i^2} \\ &= (N_x N_y)^2 f_T f_d \end{aligned}$$

where “~” means equivalent in a statistical sense and we have defined $f_T \equiv \frac{1}{N_x N_y} \sum_p^{N_x} \sum_q^{N_y} (w_{pq}^i)^2$, $f_d \equiv \frac{1}{N_x N_y} \sum_p^{N_x} \sum_q^{N_y} (d_{pq}^i)^2$. When no tapering is applied, the right-hand side (RHS) above becomes $(N_x N_y)^2 f_d$. The Plancherel relation (*) above becomes

$$f_T f_d \simeq \frac{1}{(N_x N_y)^2} \sum_{m=-N_x/2+1}^{N_x/2} \sum_{n=-N_y/2+1}^{N_y/2} |\tilde{d}^i(k_m, l_n)|^2 = \frac{1}{N_x N_y} \overline{|\tilde{d}^i|^2} \quad .$$

Since the mean of a χ^2 distribution is equivalent to the number of elements summed and the variance is twice the mean, we have $\overline{\phi^i}/c = 2$ or 1 and $\sigma_{\phi^i}^2/c^2 = 4$ or 2 where $\phi^i \equiv |\tilde{d}^i|^2$ and c is the normalization factor. Thus,

$$c = \frac{N_x N_y f_T f_d}{2} \quad (2 \leq i \leq N/2)$$

$$c = N_x N_y f_T f_d \quad (i = 1, N/2 + 1)$$

so $\phi^i/c (\equiv \Phi)$ follows the χ^2 distribution. Since, $\Phi(k_r)$ are normalized to the χ^2 distribution, the probability that the estimated spectrum $\Phi^{est}(k_{r_m})$ should be close to the true spectrum $\Phi^{true}(k_{r_m})$ is:

$$p\left(\frac{2\nu\Phi^{est}(k_{r_m})}{b} \leq \Phi^{true}(k_{r_m}) \leq \frac{2\nu\Phi^{est}(k_{r_m})}{a}\right) = 1 - \alpha$$

(Gille (2015)) where $1 - \alpha$ is the confidence level (i.e. $\alpha = 0.05$ for 95% confidence). a and b are the $(1 - \alpha)/2$ and $\alpha/2$ critical values of the $\chi^2(2\nu)$ distribution and ν ($\equiv NM(r)$) is the number of chunks that are added up. The $p\%$ confidence range therefore is:

$$\frac{2\nu}{b} \leq \frac{\Phi^{true}(k_{r_m})}{\Phi^{est}(k_{r_m})} \leq \frac{2\nu}{a} .$$

Thus

$$\log(\Phi^{est}(k_{r_m})) + \log\left(\frac{2\nu}{b}\right) \leq \log(\Phi^{true}(k_{r_m})) \leq \log(\Phi^{est}(k_{r_m})) + \log\left(\frac{2\nu}{a}\right)$$

so the confidence interval is:

$$error_{high} = \log\left(\frac{2\nu}{a}\right), \quad error_{low} = \log\left(\frac{2\nu}{b}\right)$$

and to move the error bar around in the log-log dimension, we can multiply the values inside the logarithm by an arbitrary factor A .

625 *A .5. Dissipation range*

The biharmonic momentum dissipation terms are calculated as defined in the POP simulation,

$$D_H(u) = \nabla^2(A_M \nabla^2 u)$$

where

$$\begin{aligned} \nabla^2 u &= \Delta_x \delta_x \frac{\Delta_y \delta_x u}{UAREA} + \Delta_y \delta_y \frac{\Delta_x \delta_y u}{UAREA} \\ &\quad - u [\delta_x k_x - \delta_y k_y + 2(k_x^2 + k_y^2)] + 2k_y \delta_x v - 2k_x \delta_y v. \end{aligned}$$

The coefficients k_x and k_y are the metric terms which arise when converting Cartesian coordinates to spherical coordinates. For further details of the definition of each variable, refer to *Smith et al.* (2010). We define the dissipation range the wavenumber above which 80% of the KE dissipation occurs, i.e.

$$0.8 = \frac{\int_{K_{diss}}^{K_{Ny}} [\check{u} \check{D}_H(u) + \check{v} \check{D}_H(v)] dK}{\int_{K_{min}}^{K_{Ny}} [\check{u} \check{D}_H(u) + \check{v} \check{D}_H(v)] dK}$$

626 where K_{Ny} , K_{min} , and K_{diss} are the Nyquist wavenumber, minimum wavenumber defined
 627 by the domain and the wavenumber which defines the dissipation range respectively. The $(\check{\cdot})$
 628 indicates the Fourier transforms defined in eqn. (A-1).

629 *A .6. Linear stability calculation*

The oceanmodes package solves the inviscid QG equations linearized around the mean background state ($u_g = -\frac{\partial \Psi}{\partial y}$, $v_g = \frac{\partial \Psi}{\partial x}$, N^2 , Q):

$$\frac{\partial q}{\partial t} + \mathbf{u}_g \cdot \nabla q + \mathbf{u} \cdot \nabla Q = 0$$

with the boundary condition of

$$\frac{\partial b}{\partial t} + \mathbf{u}_g \cdot \nabla b + \mathbf{u} \cdot \nabla (B + N^2 \eta) = 0$$

where a plane-wave solution for the perturbation, i.e. $\psi = \text{Re}[\Phi(z)e^{i(kx+ly-\omega t)}]$ is assumed and η is the topographic slope. The velocity field is divided into the geostrophic and perturbation component. The geostrophic velocity \mathbf{u}_g is derived as

$$\mathbf{u}_g = \frac{g}{f\rho_{ref}} [\bar{\rho} \mathbf{e}_z \times \nabla \eta + (\eta - z) \mathbf{e}_z \times \nabla \bar{\rho}]$$

where $\bar{\rho} \equiv \int_{-H}^0 \rho(z) dz$ and \mathbf{e}_z is the unit vector along the vertical axis. The reference density (ρ_{ref}) is taken to be the potential density at the surface.

$$q = \nabla^2 \psi + \Gamma \psi, \quad Q = \beta y + \Gamma \Psi$$

$$b = f \frac{\partial \psi}{\partial z}, \quad B = f \frac{\partial \Psi}{\partial z} \left(= \int N^2(z) dz \right)$$

are the perturbed and mean QG potential vorticity (QGPV) and buoyancy respectively where
 $\Gamma \equiv \frac{\partial}{\partial z} \left(\frac{f^2}{N^2} \frac{\partial}{\partial z} \right)$. The buoyancy frequency (N^2) was derived using the gsw Python package (
<https://github.com/TEOS-10/python-gsw> (*McDougall and Barker, 2011*)).

Starting from the linearized QG potential vorticity equation around a state of rest ($\mathbf{u}_g = 0$) and prescribing a solution as $\Psi = \text{Re}[e^{i(kx+ly-\sigma t)}] \Phi(z)$, we get:

$$\begin{aligned} 0 &= \frac{\partial}{\partial t} \left[\nabla_z^2 \Psi + \frac{\partial}{\partial z} \left(\frac{f^2}{N^2} \frac{\partial \Psi}{\partial z} \right) \right] + \beta \frac{\partial \Psi}{\partial x} \\ &= i\sigma \left[(k^2 + l^2) e^{i(kx+ly-\sigma t)} \Phi - e^{i(kx+ly-\sigma t)} \frac{d}{dz} \left(\frac{f^2}{N^2} \frac{d\Phi}{dz} \right) \right] + ike^{i(kx+ly-\sigma t)} \beta \Phi \end{aligned}$$

633

$$\Gamma \Phi \equiv \frac{d}{dz} \left(\frac{f^2}{N^2} \frac{d\Phi}{dz} \right) = - \left(k^2 + l^2 + \frac{k}{\sigma} \beta \right) \Phi \equiv -K^2 \Phi \quad (\text{A-2})$$

where K is defined as 2π over wavelength, which is often referred as "Rossby deformation wavenumber". Assuming the same conditions as in *Smith (2007)* and taking caution of the vertical layer setup in the POP model (Fig. 20), we can discretize the equation above as:

$$\Gamma_n^m \Phi_n = \frac{f^2}{\delta_n} \left(\frac{1}{N_n^2} \frac{\Phi_{n+1} - \Phi_n}{\Delta_n} - \frac{1}{N_{n-1}^2} \frac{\Phi_n - \Phi_{n-1}}{\Delta_{n-1}} \right) \quad (1 < n < \nu)$$

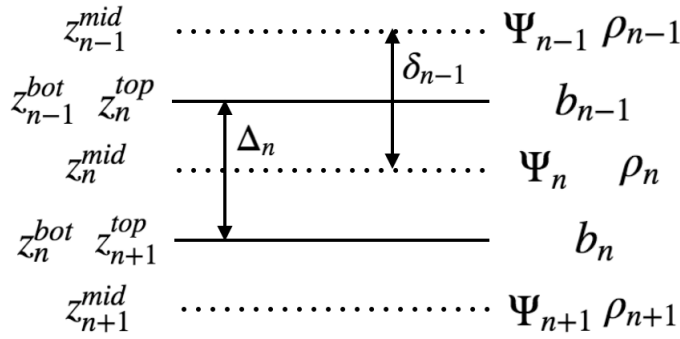


Figure 20: The vertical layer setup of the POP model. The stream function (Ψ) and density (ρ) are defined at the midpoint of each vertical layer and buoyancy (b, N) is defined on the boundaries of each layer.

$$\Gamma_1^m \Phi_1 = \frac{f^2}{\delta_1} \left(\frac{1}{N_1^2} \frac{\Phi_2 - \Phi_1}{\Delta_1} \right)$$

$$\Gamma_\nu^m \Phi_\nu = \frac{f^2}{\delta_\nu} \left(\frac{-1}{N_{\nu-1}^2} \frac{\Phi_\nu - \Phi_{\nu-1}}{\Delta_{\nu-1}} \right)$$

634 where the superscript m and subscript n ($= 1, 2, \dots, \nu$) represent the eigenmodes and vertical
 635 layer respectively.

636 References

- 637 Arbic, B. K., K. L. Polzin, R. B. Scott, J. G. Richman, and J. F. Shriver, On eddy viscosity,
 638 energy cascades, and the horizontal resolution of gridded satellite altimeter products, *Journal
 639 of Physical Oceanography*, 43, 283–300, 2013.
- 640 Arbic, B. K., M. Müller, J. G. Richman, J. F. Shriver, A. J. Morten, R. B. Scott, G. Sérazin,
 641 and T. Penduff, Geostrophic turbulence in the frequency–wavenumber domain: Eddy-driven
 642 low-frequency variability*, *Journal of Physical Oceanography*, 44, 2050–2069, 2014.
- 643 Blumen, W., Uniform potential vorticity flow: Part i. theory of wave interactions and two-
 644 dimensional turbulence, *Journal of the Atmospheric Sciences*, 35, 774–783, 1978.
- 645 Boccaletti, G., R. Ferrari, and B. Fox-Kemper, Mixed layer instabilities and restratification,
 646 *Journal of Physical Oceanography*, 37, 2228–2250, 2007.
- 647 Brannigan, L., D. Marshall, A. Naveira-Garabato, and A. Nurser, The seasonal cycle of subme-
 648 soscale flows, *Ocean Modelling*, 2015.

- 649 Buckingham, C. E., et al., Seasonality of submesoscale flows in the ocean surface boundary
650 layer, *Geophysical Research Letters*, 43, 2118–2126, 2016.
- 651 Bühler, O., J. Callies, and R. Ferrari, Wave-vortex decomposition of one-dimensional ship-
652 track data, *Journal of Fluid Mechanics*, 756, 1007, 2014.
- 653 Callies, J., and R. Ferrari, Interpreting energy and tracer spectra of upper-ocean turbulence in
654 the submesoscale range (1–200 km), *Journal of Physical Oceanography*, 43, 2456–2474,
655 2013.
- 656 Callies, J., R. Ferrari, J. Klymak, and J. Gula, Seasonality in submesoscale turbulence, *Nature
657 communications*, 6, 2015.
- 658 Callies, J., G. Flierl, R. Ferrari, and B. Fox-Kemper, The role of mixed-layer instabilities in
659 submesoscale turbulence, *Journal of Fluid Mechanics*, 788, 5–41, 2016.
- 660 Capet, X., J. McWilliams, M. Molemaker, and A. Shchepetkin, Mesoscale to submesoscale
661 transition in the California current system. part ii: Frontal processes, *Journal of Physical
662 Oceanography*, 38, 44–64, 2008a.
- 663 Capet, X., J. C. McWilliams, M. J. Molemaker, and A. F. Shchepetkin, Mesoscale to subme-
664 soscale transition in the California current system. part iii: Energy balance and flux, *Journal
665 of Physical Oceanography*, 38, 2256–2269, 2008b.
- 666 Charney, J., Geostrophic turbulence, *Journal of the Atmospheric Sciences*, 28, 1087–1095,
667 1971.
- 668 Chen, R., A. F. Thompson, and G. R. Flierl, Time-dependent eddy-mean energy diagrams and
669 their application to the ocean, *Journal of Physical Oceanography*, 46, 2827–2850, 2016.
- 670 de Boyer Montégut, C., G. Madec, A. S. Fischer, A. Lazar, and D. Iudicone, Mixed layer
671 depth over the global ocean: An examination of profile data and a profile-based climatology,
672 *Journal of Geophysical Research: Oceans*, 109, 2004.

- 673 Dufau, C., M. Orsztynowicz, G. Dibarboure, R. Morrow, and P.-Y. Le Traon, Mesoscale reso-
 674 lution capability of altimetry: Present and future, *Journal of Geophysical Research: Oceans*,
 675 *121*, 4910–4927, 2016.
- 676 Eady, E. T., Long waves and cyclone waves, *Tellus*, *1*, 33–52, 1949.
- 677 Fox-Kemper, B., and R. Ferrari, Parameterization of mixed layer eddies. part ii: Prognosis and
 678 impact, *Journal of Physical Oceanography*, *38*, 1166–1179, 2008.
- 679 Fox-Kemper, B., R. Ferrari, and R. Hallberg, Parameterization of mixed layer eddies. part i:
 680 Theory and diagnosis, *Journal of Physical Oceanography*, *38*, 1145–1165, 2008.
- 681 Fu, L.-L., and R. Ferrari, Observing oceanic submesoscale processes from space, *Eos (Washington. DC.)*, *89*, 488, 2008.
- 682 Gill, A., J. Green, and A. Simmons, Energy partition in the large-scale ocean circulation and
 683 the production of mid-ocean eddies, in *Deep Sea Research and Oceanographic Abstracts*,
 684 vol. 21, pp. 499–528, Elsevier, 1974.
- 685 Gille, S., Spectral uncertainties, <http://www-pord.ucsd.edu/~sgille/sio221c/lectures/spectra.pdf>,
 686 2015.
- 687 Griffies, S. M., et al., Impacts on ocean heat from transient mesoscale eddies in a hierarchy of
 688 climate models, *Journal of Climate*, *28*, 952–977, 2015.
- 689 Gula, J., M. J. Molemaker, and J. C. McWilliams, Submesoscale cold filaments in the gulf
 690 stream, *Journal of Physical Oceanography*, *44*, 2617–2643, 2014.
- 691 Hallberg, R., Using a resolution function to regulate parameterizations of oceanic mesoscale
 692 eddy effects, *Ocean Modelling*, *72*, 92–103, 2013.
- 693 Held, I., R. Pierrehumbert, S. Garner, and K. Swanson, Surface quasi-geostrophic dynamics,
 694 *Journal of Fluid Mechanics*, *282*, 1–20, 1995.
- 695 Holland, W. R., The role of mesoscale eddies in the general circulation of the ocean-numerical
 696 experiments using a wind-driven quasi-geostrophic model, *Journal of Physical Oceanogra-
 697 phy*, *8*, 363–392, 1978.

- 699 Hoskins, B., The mathematical theory of frontogenesis, *Annual review of fluid mechanics*, 14,
 700 131–151, 1982.
- 701 Jayne, S., and J. Marotzke, The oceanic eddy heat transport*, *Journal of Physical Oceanogra-*
 702 *phy*, 32, 3328–3345, 2002.
- 703 Lapeyre, G., and P. Klein, Dynamics of the upper oceanic layers in terms of surface quasi-
 704 geostrophy theory, *Journal of physical oceanography*, 36, 165–176, 2006.
- 705 Large, W., J. McWilliams, S. Doney, et al., Oceanic vertical mixing: A review and a model with
 706 a nonlocal boundary layer parameterization, *Reviews of Geophysics*, 32, 363–404, 1994.
- 707 Lévy, M., P. Klein, A. Tréguier, D. Iovino, G. Madec, S. Masson, and K. Takahashi, Modifica-
 708 tions of gyre circulation by sub-mesoscale physics, *Ocean Modelling*, 34, 1–15, 2010.
- 709 McClean, J., et al., A prototype two-decade fully coupled fine-resolution CCSM simulation,
 710 *Ocean Modelling*, 39, 10–30, 2011.
- 711 McDougall, T., and P. Barker, Getting started with teos-10 and the gibbs seawater (gsw) oceano-
 712 graphic toolbox, *SCOR/IAPSO WG*, 127, 1–28, 2011.
- 713 McWilliams, J. C., Submesoscale currents in the ocean, in *Proc. R. Soc. A*, vol. 472, p.
 714 20160117, The Royal Society, 2016.
- 715 Menke, W., and J. Menke, *Environmental data analysis with MATLAB*, Elsevier, 2009.
- 716 Mensa, J., Z. Garraffo, A. Griffa, T. Özgökmen, A. Haza, and M. Veneziani, Seasonality of the
 717 submesoscale dynamics in the gulf stream region, *Ocean Dynamics*, 63, 923–941, 2013.
- 718 Qiu, B., S. Chen, P. Klein, H. Sasaki, and Y. Sasai, Seasonal mesoscale and submesoscale eddy
 719 variability along the north pacific subtropical countercurrent, *Journal of Physical Oceanog-
 720 raphy*, 44, 3079–3098, 2014.
- 721 Rhines, P. B., Geostrophic turbulence, *Annual Review of Fluid Mechanics*, 11, 401–441, 1979.

- 722 Rocha, C. B., T. K. Chereskin, S. T. Gille, and D. Menemenlis, Mesoscale to submesoscale
 723 wavenumber spectra in drake passage, *Journal of Physical Oceanography*, 46, 601–620,
 724 2016a.
- 725 Rocha, C. B., T. K. Chereskin, S. T. Gille, and D. Menemenlis, Seasonality of submesoscale
 726 dynamics in the kuroshio extension, *Geophysical Research Letters*, 2016b.
- 727 Sasaki, H., P. Klein, B. Qiu, and Y. Sasai, Impact of oceanic-scale interactions on the seasonal
 728 modulation of ocean dynamics by the atmosphere, *Nature communications*, 5, 2014.
- 729 Schloesser, F., P. Cornillon, K. Donohue, B. Boussidi, and E. Iskin, Evaluation of thermos-
 730 alinograph and viirs data for the characterization of near-surface temperature fields, *Journal*
 731 *of Atmospheric and Oceanic Technology*, 33, 1843–1858, 2016.
- 732 Small, R., et al., A new synoptic scale resolving global climate simulation using the community
 733 earth system model, *Journal of Advances in Modeling Earth Systems*, 6, 1065–1094, 2014.
- 734 Smith, R., et al., The parallel ocean program reference manual, 2010.
- 735 Smith, S., The geography of linear baroclinic instability in earth's oceans, *Journal of Marine*
 736 *Research*, 65, 655–683, 2007.
- 737 Stammer, D., Global characteristics of ocean variability estimated from regional
 738 topex/poseidon altimeter measurements, *Journal of Physical Oceanography*, 27, 1743–1769,
 739 1997.
- 740 Thomas, L., A. Tandon, and A. Mahadevan, Submesoscale processes and dynamics, *Ocean*
 741 *Modeling in an Eddying Regime*, *Geophys. Monogr. Ser.*, 177, 17–38, 2008.
- 742 Vallis, G. K., *Atmospheric and oceanic fluid dynamics: fundamentals and large-scale circula-*
 743 *tion*, Cambridge University Press, 2006.
- 744 Volkov, D., T. Lee, and L. Fu, Eddy-induced meridional heat transport in the ocean, *Geophysi-*
 745 *cal Research Letters*, 35, 2008.

⁷⁴⁶ Xu, Y., and L. Fu, Global variability of the wavenumber spectrum of oceanic mesoscale turbulence, *Journal of physical oceanography*, 41, 802–809, 2011.

⁷⁴⁸ Xu, Y., and L. Fu, The effects of altimeter instrument noise on the estimation of the wavenumber spectrum of sea surface height, *Journal of Physical Oceanography*, 42, 2229–2233, 2012.

ACCEPTED MANUSCRIPT